

Abstract

Title of Document:

**PROGRESSIVE MICROSCOPIC DAMAGE
AND THE DEVELOPMENT OF
MACROSCOPIC FRACTURE IN
POROUS SANDSTONES**

Thomas F. Tamarkin, Master of Science, 2011

Directed By:

Assistant Professor, Dr. Wenlu Zhu, Geology

The precursory phenomena associated with dilatancy have been extensively studied as a potential means of earthquake prediction. It is known that microstructural damage induced dilatancy precedes macroscopic failure of a rock. However, the quantitative relationship between microstructural damage and fault development is not clearly understood. To better understand the mechanics of brittle faulting of rock and the association of precursory phenomena with faulting, a detailed microstructural study was conducted on porous sandstone deformed to different post-failure stages at different strain rates. A lateral relaxation loading configuration was adopted in which a cylindrical sample is deformed under decreasing radial stresses while the axial load remains constant. This loading path was proven to successfully map out the brittle failure envelope. Compared to conventional triaxial deformation testing, the relaxation loading configuration greatly increases the stability of fault growth. A suite of samples were deformed and subsequently unloaded at different post-failure stages, before macroscopic faulting occurred. Progressive microstructural damage was investigated via quantitative characterization of crack damage indices, crack density, and changes in porosity. Ultimately, this research will lead to an improved comprehension of the relationship between microscopic damage and macroscopic fracture development, providing a better insight into the brittle failure process.

PROGRESSIVE MICROSCOPIC DAMAGE AND THE
DEVELOPMENT OF MACROSCOPIC FRACTURE IN POROUS
SANDSTONES

By

Thomas F. Tamarkin

Thesis submitted to the Faculty of the Graduate School of the
University of Maryland, College Park, in partial fulfillment
of the requirements for the degree of
Master of Science
2011

Advisory Committee:
Professor Dr. Wenlu Zhu, Chair
Dr. Laurent Montési
Dr. Andrew Campbell

© Copyright by
Thomas F. Tamarkin
2011

Table of Contents

Abstract	
Table of Contents	ii
List of Tables	iii
List of Figures	iv
Chapter 1: Introduction	1
Chapter 2: Experimental Setup: Triaxial Deformation Apparatus and Sample Preparation	5
2.1 Operating Principle of Transducers	7
2.1.1 Linear Variable Differential Transducers (LVDTs)	7
2.1.2 Pressure transducers	9
2.2 Triaxial Deformation Apparatus	11
2.2.1 Load Cell	12
2.2.2 Main Hydraulic Ram	14
2.2.3 Confining Pressure Intensifier	15
2.2.4 Pore Pressure Intensifier	15
2.3 Sample Assembly	17
2.3.1 Application of Copper Foil	17
2.3.2 Attachment of Strain Gages	18
2.3.3 Strain Gage Conditioning	19
2.4 Calibration of Stress and Strain Measurements	20
Chapter 3: Progressive Development of Brittle Faulting: Deformation Tests	24
3.1: Conventional Loading Path	25
3.2: Lateral Relaxation Loading Path	26
3.2.1: Mohr's Circle	28
3.3: Strain Rates	30
3.4: Faulting Energy	34
Chapter 4: Progressive Development of Brittle Faulting: Microstructural Analysis	37
4.1 Characterization of Microscopic Damage: Damage Index	39
4.2 Quantification of Microcrack Density	43
Chapter 5: Conclusions	52
Appendices	55
A.1 LVDT Calibration Plots	55
A.2 Nominal Crack Density Calculation	56
A.3 Standardization and Verification of Matlab technique	57
A.4 Matlab code for image analysis: Grain Area	59
A.5 Matlab code for image analysis: Feature Boundary	62
References	66

List of Tables

Table 2.1 List of sensors on the triaxial deformation apparatus and the corresponding ranges and precisions.	16
Table 3.1: Experimental results from lateral relaxation loading of Darley Dale sandstone at two different strain rates. dd-09 and dd-10 were removed prior to macroscopic fault development and dd-17 is the only sample run using the conventional loading path.....	35

List of Figures

Figure 2.1: Triaxial deformation apparatus with confining and pore pressure intensifiers shown. Axial (red) and radial (yellow) stresses shown on enlarged sample view. ...	6
Figure 2.2: Main hydraulic ram LVDT calibration. Slope of best fit line is used to determine displacement from output voltage during experimental runs.	9
Figure 2.3: Labeled diagram of a typical strain gage (Image from Vishay, 2003) (Active grid length of gauges used is 0.95 cm (0.375 inches)).....	11
Figure 2.4: Top and side view of custom hollow load cell.	12
Figure 2.5: Schematic representation of an a) full bridge Wheatstone bridge circuit composed of 4 strain gages; two in compression and two in Tension and b) a quarter bridge Wheatstone bridge circuit. Adapted from Horowitz and Hill (1989).....	13
Figure 2.6: Cylindrical 2024 aluminum sample (2.54 cm in diameter) with axial and radial strain gages attached.	19
Figure 2.7a: Deformation of a 2024 aluminum sample: Poisson ratio 0.33 (confining pressure=40 MPa).	22
Figure 2.7b: Hydrostatic compaction of a 2024 aluminum sample: Bulk modulus 87.5 GPa.....	22
Figure 2.7c: Deformation of a 2024 aluminum sample: Young’s modulus 76.6 GPa.....	23
Figure 3.1: A typical differential stress- axial strain curve of a rock undergone brittle failure with the failure process divided into 5 different stages showing yield softening behavior (after Wawersik and Brace, 1971; Scholz, 2002).	25
Figure 3.2: Comparison of a conventional loading path to that of the lateral relaxation loading path used in this study (after Zhu et al. 2003).....	27
Figure 3.3: a) Stress-strain curve of a Darley Dale sandstone sample (dd-17) deformed at effective pressure of 70MPa using the conventional loading configuration. The 5 deformation stages are indicated; b) Volumetric strain as a function of axial strain during deformation. The onset of dilatancy is marked by the change in compaction rate (C’). Strain gages were destroyed by the shear fracture developed in stage V, shortly after sample reached its peak stress.	27
Figure 3.4: Stress states in a rock sample deformed a) under conventional triaxial compression loading; b) under lateral relaxation triaxial compressional loading, using Mohr’s circle. The Coulomb-Mohr failure criterion is also shown. Dashed Mohr’s circles represent intermediate stress state during deformation. Solid Mohr’s circle represents the stress state at failure.	28
Figure 3.5: Comparison of the mechanical data between sample dd-05 deformed under the lateral relaxation loading configuration (at effective pressure $P_0=190$ MPa) and sample dd-17 deformed under the conventional loading configuration (at $P_0=70$ MPa). a) stress-strain curve; b) radial strain vs. axial strain; c) volumetric strain vs. axial strain.....	31
Figure 3.6: Comparison of mechanical data of dd-08 and dd-10, deformed at a strain rate of $5.5 \times 10^{-6} \text{ s}^{-1}$. Sample dd-08 underwent considerable strain soften and a	

macroscopic shear fracture is developed, whereas sample dd-10 was unloaded shortly after reaching the peak stress, no macroscopic shear fracture is observed. a) stress strain curve; b) axial strain over time; c) volumetric strain vs. axial strain.... 32

Figure 3.7: a) Post failure sample (dd-08) with obvious shear localization and b) schematic diagram showing the relations between the orientation of shear fracture plane and the principal stress directions. 33

Figure 3.8: Mechanical data from sample dd-05 (strain rate of $5.5 \times 10^{-6} \text{ s}^{-1}$) and dd-06 (strain rate of $2.5 \times 10^{-6} \text{ s}^{-1}$) a) stress-strain curve; b) axial strain over time c) volumetric strain vs. axial strain. 34

Figure 3.9: Transformation of a) experimental deformation data to infer b) the shear stress verses relative fault slip allowing the fracture energy to be measured as the area under the shear vs. fault slip curve. 35

Figure 4.1: Plots of acoustic emissions during shear localization of sample (Lockner et al. 1992) 38

Figure 4.2: A reflected light image of the four DDL thin sections. Corresponding effective pressure used in the deformation test for that sample is indicated next to sample label. Nominal strain rate is $\sim 5 \times 10^{-5} / \text{s}$ 40

Figure 4.3: Loading paths for DDL45, DDL46, DDL47 and DDL49. Deformation stages I-V (see Figure 3.1) are indicated (After Zhu et al. 2003). 40

Figure 4.4: Damage index developed by Menéndez et al.(1996) and associated color scheme used. 41

Figure 4.5a: Reflected light image of the 4 experimental DDL runs with corresponding damage index all 4 DDL samples have a 1.84 cm (0.725 inch) diameter (shorter dimension of thin section). b) Reflected light image of dd-00 the undeformed control with 2.54 cm (1 inch) diameter (shorter dimension of thin section). 42

Figure 4.6: Loading paths for dd-04, dd-05, dd-06, dd-08, dd-09, and dd-10. Deformation stages I-V (see Figure 3.1) are indicated. 44

Figure 4.7: Reflected light image of the 6 experimental runs a) dd-00 undeformed control b) dd-04 run at a strain rate of $1.8 \times 10^{-6} \text{ s}^{-1}$: dd-06, and dd-09 run at a strain rate of $2.5 \times 10^{-6} \text{ s}^{-1}$ and c) dd-05, dd-08, and dd-10 run at a strain rate of $5.5 \times 10^{-6} \text{ s}^{-1}$ with corresponding damage index. All samples have a 2.54 cm (1 inch) diameter (shorter dimension of thin section). 44

Figure 4.8: Crack density analysis and image binarization. Black pixels are converted to binary “1”s and white to “0”s. Sum array is made from circular image and white line at a desired angle of investigation. Then search for the number of “2”s in the newly created array. 47

Figure 4.9: Example of location where samples were trimmed by the thin section company. None of the areas with obvious failures were trimmed away. 48

Figure 4.10: Matlab function “edgeimage” identifies the edges of grains and cracks within the grains. 49

Figure 4.11: Nominal crack density of all samples. The areas of maximum damage were analyzed at all angles and the maximum crack density of all of these values was chosen to identify the maximum amount of damage in that portion of the thin section. In regards to the minimum values for each sample, a crack density of 2 indicates that there is no damage to the grain since this represents 2 edges per grain. The minimum damaged areas were averaged over all angles since there was no

preferred damage orientation. The shaded area is the undeformed sample dd-00 (Tamarkin and Zhu, 2009).	50
Figure A-1: Pore pressure intensifier LVDT calibration plot.....	55
Figure A-2: Formula for calculation of nominal crack density	56
Figure A-3 a) and 3b: Random area selected for technique verification. b) Figure A-3a rotated 45° (Both on a black back ground).	57
Figure A-3c: Comparison of image analysis from Figures A-3a and b Results are consistent indicating orientation of image does not affect crack counting software.	57
Figure A-4a: 2000 Pixel radius white circle.	58
Figure A-4b: Matlab image analysis of 2000 Pixel radius white circle indicating 2000 pixels counted at all angles from 0-180°	58

Chapter 1: Introduction

Earthquakes, along with the secondary effects of earthquakes such as tsunamis, landslides, and soil liquefaction, are natural hazards that often cause large scale damage to human society. Earthquake prediction has long been the “holy grail” of seismology (e.g., Gilbert, 1909). Most common earthquakes result from sudden motions caused by unstable slip (rupture) along the fault surface. The connection between earthquakes and dynamic faulting led to Reid’s elastic rebound theory, where an earthquake cycle is analyzed by strain accumulation and release around the fault (Reid, 1910). Based on Reid’s conception, the recurrence of large earthquakes is time predictable.

Considerable progresses have been made for long-term prediction in determination of the recurrence time of earthquakes on a specific fault segment (e.g., Shimazaki and Nakata, 1980; Bakun and McEvilly, 1984). However, short-term prediction would require the identification of precursory phenomena marking the impending earthquakes. Seismogenic faulting can be modeled as dynamic crack propagation (e.g., Haskell, 1964; Andrew, 1976; Das, 1981). Searching for precursory phenomena associated with earthquake cycles focuses on different aspects of the observable preliminary effects of faulting. For instance, monitoring of terrestrial gases in groundwater and soil reveals anomalously high concentrations of gasses such as radon, helium, and several other volatiles along some active faults, which suggests that the cracks within the rock may be paths of least resistance for the terrestrial gases generated or stored in the earth to escape to the surface (Scholz et al., 1973; King, 1986). Scholz et al. (1973) reports that the radon content in deep well water increased several fold prior to earthquakes. They hypothesize that in this specific environment, rocks along the fault

begin to dilate in response to tectonic stresses, due to opening up of cracks in their interior. Crack opening releases radon gas and the process continues until an earthquake occurs.

The loading and rupture of water-saturated crustal rocks during earthquakes, together with fluid/gas movement, stress redistribution, change in material properties, has long been expected to generate associated magnetic and electric field perturbations. The detection of related perturbations prior to fault rupture has thus been proposed as a simple and inexpensive method for monitoring the state of crustal stress and perhaps providing tools for predicting crustal failure (Brace and Orange, 1968; Park, 1991; Fenoglio, 1995; Johnston, 1997). The primary mechanisms for generation of electric and magnetic effects with crustal deformation and earthquakes effects include piezomagnetism, stress/conductivity, electrokinetic effects, charge generation and dispersion, and magnetohydrodynamic effects. During the past few decades, there has been a remarkable increase in the quality and quantity of electromagnetic data recorded before and during earthquakes (Johnston, 1997), but more work needs to be done to convincingly demonstrate to the international geophysical community, causality, or lack thereof, between electromagnetic signals and earthquakes.

Such precursory phenomena seem to be anomalous signals associated with seismogenic faulting. Without quantitative understanding of the physical mechanisms operative during the imminent stage of an earthquake, none of these methods could be used reliably in earthquake mitigation.

An earthquake results from a buildup of energy followed by a sudden release of energy during the rupture of the fault (e.g., Scholz, 2002). The rupture due to the release

of energy can also be observed in individual rocks. This macroscopic failure can occur on the centimeter scale as can be seen in a hand specimen of a deformed rock or it can occur on a much larger scale, i.e., natural faults in the earth's lithosphere up to hundreds of kilometers long, such as the San Andreas Fault.

The goal of this study is to advance the understanding of the mechanics of brittle faulting, with a focus on an improved comprehension of the relationship between microscopic damage and macroscopic fracture development. To accomplish this task, an integrated approach consisting of laboratory deformation experiments and quantitative microstructural analysis has been adopted.

Previous studies on brittle faulting processes show that dilatancy, the inelastic volume increase during deformation, is ubiquitous prior to rupture propagation (e.g., Brace, 1964). In the context of earthquake precursory phenomena, many efforts were made to constrain the point at which materials become dilatant. It is shown that the onset of dilatancy varies considerably among different rock types (e.g., Brace, 1978; Fredrich et al., 1989; Wong et al., 1997).

Despite the importance of brittle faulting in seismogenic processes, quantitative details of nucleation and propagation of brittle failure are not clearly understood (e.g., Scholz, 2002). This is partly due to the unstable nature of crack propagation. Once the conditions of brittle failure are met, fault propagation proceeds rapidly and is difficult to observe (e.g., Wawersik and Brace, 1971; Lockner et al., 1992). To circumvent this problem, I adopted an experimental loading configuration which differed from the conventional loading configuration (Zhu et al., 2003).

Using this new loading configuration, I conducted a suite of deformation experiments on Darley Dale sandstone samples. Chapter 2 features a description of the principals of a triaxial deformation apparatus and the calibrations of the sensors that are attached to the apparatus. Chapter 3 focuses on the experiments that were run and subsequently unloaded at different post-failure stages, while the focus of chapter 4 is reporting results from the microstructural analysis that was performed. This includes quantitative characterization of the progressive microstructural damage in the samples performed by examining crack density and crack damage indices to determine characteristic failure patterns. The appendices contain tables that include the specific details of each of the samples and plots which compare the results from all of the experimental runs.

Chapter 2: Experimental Setup: Triaxial Deformation Apparatus and Sample Preparation

Understanding the nucleation and propagation of brittle fracture in rocks is critical in studying earthquake mechanics because of the close correlation between the rupture propagation and the seismogenic faulting process, (Scholz, 2002). Rock deformation is controlled by the confining pressure (overburden), tectonic stress, and temperature. At pressure and temperature conditions pertinent to seismogenic zone in the crust (i.e., <15 km), stress-induced volume changes are an important aspect of deformation. Volume changes come from elastic deformation of the minerals, compaction (volume reduction) of the void space, and dilatancy, increase of void space (e.g., Brace, 1978). By varying pressure and temperature conditions, mechanisms that control the failure process can be isolated and investigated in laboratory experiments.

A programmable, servo controlled conventional triaxial deformation apparatus is used for conducting deformation tests on cylindrical samples (Figure 2.1). Using servo controlled hydraulically powered intensifiers, the confining pressure, axial load and pore fluid pressure can be applied under servo feedback control. Complete servo control minimizes fluctuations in experimental conditions which significantly improves the precision of collected data. In this chapter, I will first introduce the different sensors used for signal control, and then I will summarize the operation and calibration of the triaxial deformation apparatus as well as sample preparation and data acquisition.

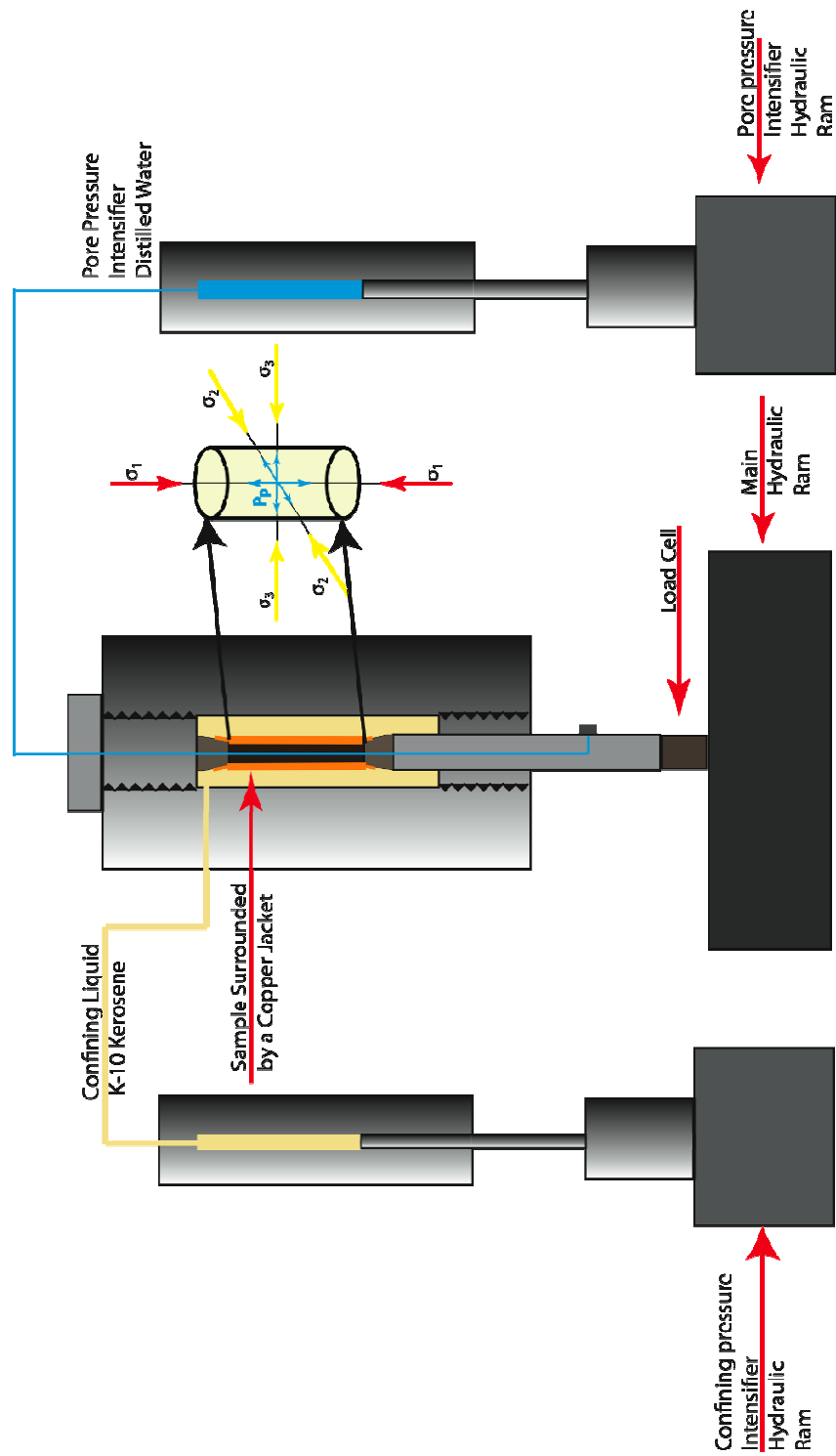


Figure 2.1: Triaxial deformation apparatus with confining and pore pressure intensifiers shown. Axial (red) and radial (yellow) stresses shown on enlarged sample view.

2.1 Operating Principle of Transducers

The servo control system is managed via feedback between sensors strategically placed on the intensifiers or in line with the intensifier system. The two types of sensors that are used on the intensifier systems are LVDTs (Linear Variable Differential Transducers) and pressure transducers.

2.1.1 Linear Variable Differential Transducers (LVDTs)

LVDTs operate on the principal that a ferromagnetic core will couple a primary coil, driven by an oscillating voltage, to a secondary coil that is wrapped around the first coil. This coupling will induce a voltage in the secondary coil. To measure displacement (or position of the ferromagnetic core within the coil assembly), the ferromagnetic core is attached to a non magnetic rod, which will pass through the primary coil freely. This rod with ferromagnetic tip is attached to the part that moves and is to be measured. The coil assembly is attached to a stationary part of the assembly and positioned so that movement of the hydraulic ram causes the rod with ferromagnetic tip to pas freely through the coil assembly. The difference in voltage between the two secondary coils results in an output voltage that is proportional to the position of the core within the coil assembly, with an output of 0 volts indicating a central or null position within the two secondary coils (Wilson and Kester, 2009). By attaching the rod with the ferromagnetic core on the equipment requiring displacement measurement, a change in output voltage of the secondary coils accurately and precisely indicates the change in displacement of the core (which is also the same displacement as the part it is attached to). The advantages of using LVDTs for measurement is that they have a theoretical infinite life because there is no contact between moving parts, output is analog with infinite resolution and allows for

easy signal conditioning, and the system will retain the position (output voltage) even if the instrument is powered off and on again.

Although the outputs from the LVDTs are reproducible, it is still necessary to calibrate them to be sure that there is not a region of nonlinearity present within the full stroke of the LVDT. There is currently no inexpensive device available to perform this necessary calibration, instead the LVDT must be sent in to the manufacturer to be calibrated. To resolve this conundrum a calibration tool was developed to perform this task. A constant rate syringe injection pump was modified to hold the coil assembly stationary while the ferromagnetic rod was attached to the injection mechanism of the syringe pump. Because the injection rate and therefore displacement rate of the injection mechanism could be controlled, the pump would advance the ferromagnetic core through the coils of the LVDT at a constant rate. This data could be recorded with the data acquisition software and plotted as time converted to displacement in microns vs. voltage. Since the pump advances the ferromagnetic core at a constant rate time is directly related to position. The calibrator will be run at a constant rate moving the core one full stroke through the LVDT. This information can be recorded and plotted to observe any nonlinearities in the LVDT. These regions of the LVDT can either be corrected for during the experiment or the LVDT positioned on the apparatus so that they are not used.

There is a LVDT attached to each of the pore pressure intensifiers, the piston for the confining pressure intensifier, and also to the main hydraulic ram applying the axial load to the sample, respectively. Calibration for the LVDT of the main ram shows that the central region is linear throughout the entire stroke of the LVDT except for the very ends of the displacement where there is a slight deviation from linearity (Figure 2.2). As

a result the LVDT was positioned on the main ram so that the displacement region of the experiment will lie within central region of the LVDT stroke, ensuring all recorded measurements will be within the linear region.

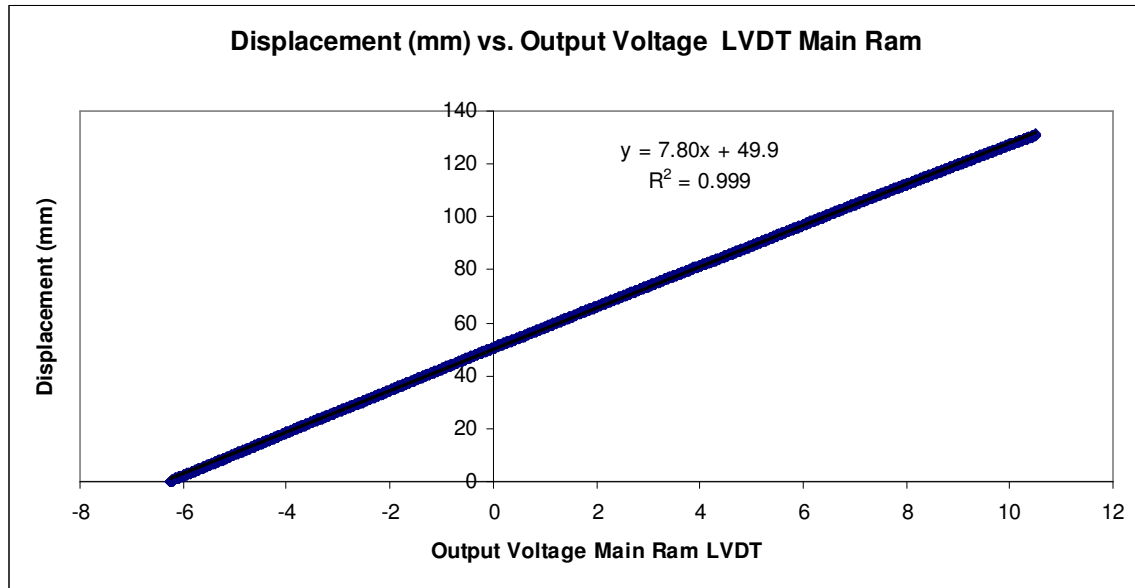


Figure 2.2: Main hydraulic ram LVDT calibration. Slope of best fit line is used to determine displacement from output voltage during experimental runs.

2.1.2 Pressure transducers

The second type of sensor used on the intensifier system is a pressure transducer. Pressure transducers are devices that are typically connected to the pressure system via high pressure tubing. The construction of the transducer involves application of a strain gauge, a device that changes resistance when deformed, to a metal diaphragm that elastically deforms as the pressure of the system changes (Dobie and Isaac, 1950). Early strain gauges were constructed from a thin wire but modern gauges are photo etched from metalized film deposited onto a polyester or plastic backing (Figure 2.3). When the gauge is strained, its resistance changes because the cross sectional area of the wires in the active portion of the gauge becomes smaller when the gauge is in tension and becomes

larger when the gage is in compression (Dobie and Isaac, 1950). The conductor wire is woven back and forth to increase the length of the wire and therefore enhances the sensitivity (gauge factor) of the strain gauge (Figure 2.3). These modern gauges can experience up to 10,000 micro strain without damage and the sensitivity of modern gauges to a given strain is typically 1% or better (Wilson and Kester, 2009).

The strain gage function within a pressure transducer is to indicate the amount of deformation that the metal diaphragm experiences as a result of a change in pressure of the system the transducer is connected to. The relationship between the deformation and the pressure change is calibrated and determined at the factory. Amplification electronics contained within the pressure transducer convert the change of resistance of the strain gauge with change in system pressure, to a voltage. This voltage can then be converted to a pressure via the factory determined linear voltage-pressure relationship factor. To validate experimental pressure conditions during machine operation, the pressure readout from the pressure transducer is compared with the mechanical, bourdon pressure tube, Heise gauge during the duration of the experiment. This ensures that the experiment is proceeding as intended.

Using a pressure transducer, the main ram can be controlled via load cell feedback where the machine will advance the ram until the load cell (and therefore sample) reaches a preset load in the servo control system. Alternatively the main ram can be controlled via displacement feedback through LVDT where the ram will advance a distance equal to the preset displacement in the servo controller. The confining pressure system is controlled via feedback from the pressure transducer, but there is also a LVDT attached to the intensifier to indicate whether intensifier piston advancement takes place during a

constant pressure system (Figure 2.1). A piston displacement during constant pressure servo control would indicate a net volume change, which could become handy for trouble shooting a leak in the system.

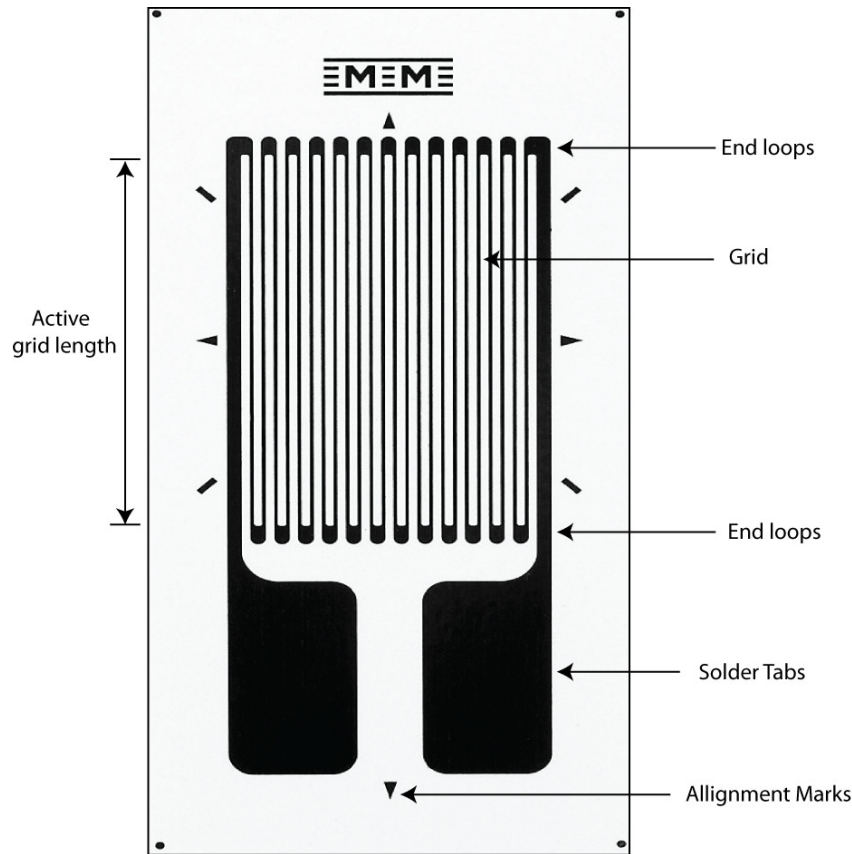


Figure 2.3: Labeled diagram of a typical strain gage (Image from Vishay, 2003) (Active grid length of gauges used is 0.95 cm (0.375 inches)).

2.2 Triaxial Deformation Apparatus

In a conventional triaxial deformation test, the axial stress σ_1 is applied to the sample via a steel piston and the radial stresses σ_2 and σ_3 are applied via a high pressure fluid surrounding the sample (Figure 2.1). Among these 3 principal stresses, σ_1 , σ_2 , and σ_3 , only 2 of them are independent (i.e., radial stresses $\sigma_2 \equiv \sigma_3$) due to the axisymmetric nature of the sample. A loading configuration with 3 identical principal stresses, i.e.,

$\sigma_1 = \sigma_2 = \sigma_3$, is called hydrostatic loading. Deformation is induced when $\sigma_1 > \sigma_2 = \sigma_3$ (triaxial compression) or $\sigma_1 < \sigma_2 = \sigma_3$ (triaxial extension).

2.2.1 Load Cell

A custom load cell was designed and constructed based on a cylindrical load-bearing member that is bored out to make a thick walled cylindrical tube (Figure 2.4). The load cell is designed to be very rugged and strong and allows an accentuated amount of elastic deformation during application of the load when compared to a load cell constructed out of a solid cylinder of material. The material that is typically used is a beryllium copper alloy or 17-4 PH stainless steel because of its high strength and similar thermal expansivity properties (Davis and Allen, 1990) to the rest of the triaxial deformation apparatus.

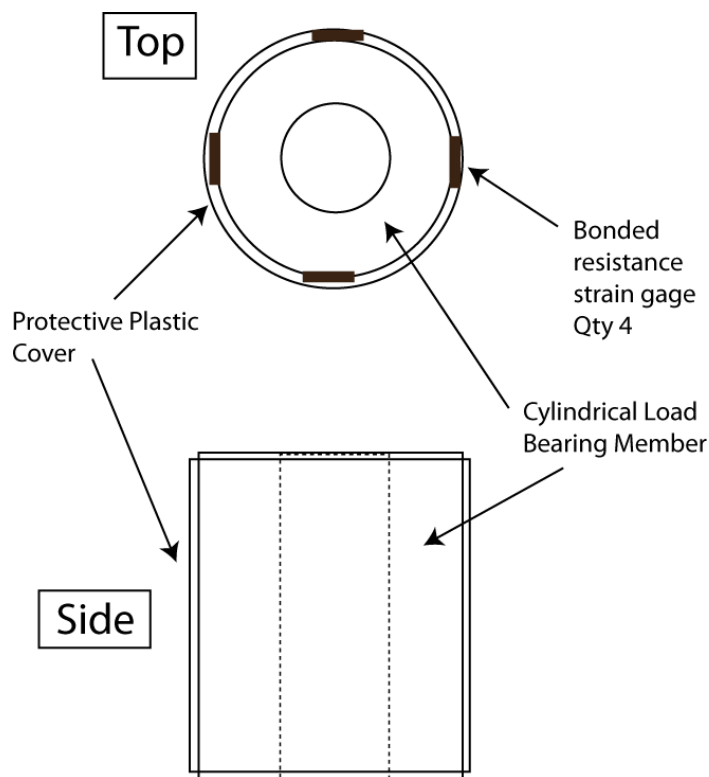


Figure 2.4: Top and side view of custom hollow load cell.

The load cell measures the amount of load applied by changes in resistance of 4 strain gages applied centrally around the circumference of the cylindrical load-bearing member (Figure 2.4). Two of the four strain gages are applied axially and the other two are applied radially. The four strain gages are then connected to a Wheatstone bridge electronic circuit (Figure 2.5a). The Wheatstone bridge is a simple electronic circuit that enables the user to measure the change in resistance of one of the resistors of the circuit, R_{gage} . R_1 , R_2 , and R_3 will be the constant resistance arms and V_o is the voltage gauge (Figure 2.5b) reading the voltage across the bridge (Dobie and Isaac, 1950). The balance in the bridge is maintained by altering R_3 , a potentiometer, so $R_{\text{gage}}/R_3=R_1/R_2$ to generate a zero or null value output on V_o (Figure 2.5b). Any subsequent change in the resistance of R_{gage} , due to strain change or other environmental factors, will result in a corresponding change in output voltage V_o . Nearly all methods of determining resistance change are based on this simple fundamental circuit. The result is that a change in resistance in the strain gages due to an application of a load will generate a change in the output voltage.

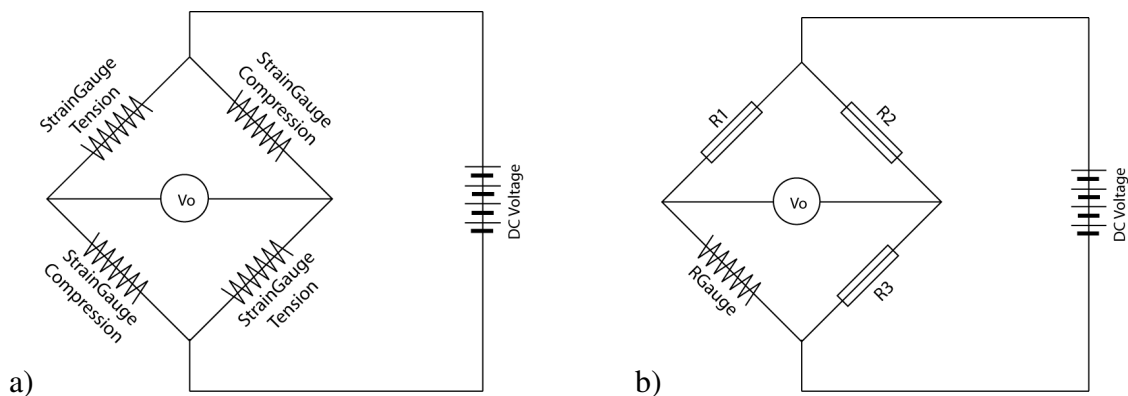


Figure 2.5: Schematic representation of an a) full bridge Wheatstone bridge circuit composed of 4 strain gages; two in compression and two in Tension and b) a quarter bridge Wheatstone bridge circuit. Adapted from Horowitz and Hill (1989).

The correlation between the applied load and the output voltage can be made through a standard load cell, significantly larger and bulkier than the custom load cell. With the assistance of a separate test frame and hand operated hydraulic cylinder the standard load cell, which is factory calibrated, is placed in series with the custom load cell and the hydraulic cylinder inside of the test frame. The hydraulic cylinder pressure is increased slightly and the system is allowed to reach thermal equilibrium. Imparting energy (pressure) to the system causes a slight temperature increase in the hydraulic fluid, which will cause a slight decrease in pressure as the system cools to thermal equilibrium. This equilibrium typically takes about 15 minutes. Once the system reaches thermal equilibrium the voltage output from the standard load cell and the custom load cell are recorded and then the pressure to the hydraulic ram is increased slightly and the process is repeated. After the output voltages of the two load cells have been recorded up to the maximum desired pressure, the process is reversed by venting the hydraulic pressure in a stepwise manner and recording the output voltages of the two load cells. The output voltage of the standard load cell is converted to a load using the factory calibrated conversion factor to obtain a useful load measurement in MPa. The slope of the best fit line between the standard load cell measurements in MPa to the output voltages of the custom load cell provides a conversion factor to convert output voltage to MPa. This procedure allows the user to determine the linearity of the load cell and the comparison of the loading slope versus the unloading slope provides the user with confidence that there is no hysteresis in the system as long as the slopes are the same.

2.2.2 Main Hydraulic Ram

The flow of high pressure, 18.6 MPa (2700 psi), hydraulic fluid to the 3 independently controlled hydraulic driven intensifiers of the triaxial deformation

apparatus is regulated via servo control (Figure 2.1). The axial stress is controlled via the main hydraulic ram, which is in series with the cylindrical sample. The main ram consists of a 35.56 cm (14 inch) diameter (d_{ram}) hydraulic ram, connected to a 3.81 cm (1.5 inch) diameter (d_{piston}) piston and then further necked down to the final 2.54 cm (1 inch) diameter (d_{sample}) sample. The stress ratio can be calculated for any intensifier using the following formula: Stress ratio $= (d_{\text{ram}} / d_{\text{sample}})^2$. Thus the application of 18.6 MPa (2700 psi) to the diameter main ram hydraulic piston results in a maximum axial stress (σ_1) that can be applied to the 2.54 cm (1 inch) diameter sample of 3647 MPa (529,000 psi).

2.2.3 Confining Pressure Intensifier

The radial stresses ($\sigma_2 = \sigma_3$) are applied to the sample generated by pumping high pressure confining medium into the load cell through a pressure intensifier (Figure 2.1). K-10 kerosene is chosen for the confining fluid in the confining fluid intensifier system because of its low vapor pressure, low viscosity, non corrosive properties, and relatively minimal compressibility (e.g., Bridgman 1958; Scholz and Koczynski, 1979).

The confining pressure intensifier is a piston cylinder system with a 1.27 cm ($\frac{1}{2}$ inch) diameter piston placed atop a 10.16 cm (4 inch) diameter hydraulic ram. The ram pushes on the piston, via servo control, compressing the fluid in the piston cylinder intensifier system. The confining pressure system has a potential of generating a maximum pressure of 1191 MPa (172,800 psi) when 18.6 MPa (2700 psi) of hydraulic pressure is applied to hydraulic ram, based on the ratio of the two cross sectional areas.

2.2.4 Pore Pressure Intensifier

The final major component of the triaxial deformation apparatus is the pore pressure intensifier, which is identical in function and appearance to the confining pressure system (Figure 2.1.) The intensifier piston diameter of the pore pressure intensifier is approximately 2.54 cm (1 inch) in diameter. With the 2.54 cm (1 inch) diameter intensifier piston and 10.16 cm (4 inch) hydraulic ram, a maximum pore pressure of 296.5 MPa (43,000 psi) can be obtained. Compared to the confining pressure intensifier, a larger diameter of the piston allows for a larger volume of pore fluid and lower maximum pressure. Although only one pore pressure intensifier was used for this study, there are two pore pressure intensifiers connected to the triaxial deformation apparatus for flow through experiments. One intensifier (pore pressure top) is connected to the sample via the top of the triaxial deformation apparatus (This is what was used for this suite of experiments), and the other (pore pressure bottom) enters the sample via the bottom of the machine (Figure 2.1).

The precision of the different sensors used on the triaxial deformation apparatus are shown in Table 2.1.

Sensor	Range and Precision
confining pressure:	345 ± 0.9 MPa ($50,000 \pm 125$ p.s.i.)
main ram displacement:	154 ± 0.8 mm (6 ± 0.03 in)
load cell-main ram:	3647 ± 4 MPa ($529,000 \pm 500$ p.s.i.)
pore fluid pressure:	69 ± 0.08 MPa ($10,000 \pm 11$ p.s.i.)
pore volumometer:	61.86 ± 0.31 cm ³ (3.775 ± 0.019 in ³)
strain gauge:	350 ± 1.05 ohm

Table 2.1 List of sensors on the triaxial deformation apparatus and the corresponding ranges and precisions.

2.3 Sample Assembly

2.3.1 Application of Copper Foil

The samples tested in this study are right cylinders with a diameter of 2.54 cm (1 inch) and a length of 5.08 cm (2 inches). All surfaces were precision ground to strict tolerances to ensure the ends are parallel and the edges are square. A copper foil jacket is used to prevent confining fluid entering the pore space of the sample. The copper foil is 0.0127 cm (0.005 inches) thick and is cut so that it will wrap around the sample, be flush at the top and bottom of the cylindrical sample and with a small overlap along the length of the sample. The seam is then soldered together to ensure a pressure tight seal along the length of the sample. Any extra solder is removed mechanically either by filing or by sanding to be sure that the transition between copper foil and solder joint is smooth and will not effect proper sealing of the rubber jacketing material. At this point, all of the exposed copper is rinsed with a solvent such as acetone or isopropyl alcohol to remove any grease or foreign contamination from the surface of the copper. The surface of the copper foil is lightly roughed up with 600 grit wet dry sanding paper and then rinsed again with solvent to remove any sanding particulates. Next, the midline of the sample is marked along the circumference of the cylinder by lightly scribing a line into the copper foil. Then, two vertical lines are scribed into the copper foil approximately 1/3 of the circumference apart from each other. The sample has now been properly prepped for strain gage attachment.

2.3.2 Attachment of Strain Gages

Two strain gages were attached to the sample to measure deformation: one parallel (referred to as the axial strain gage) with the long axis of the sample, and the other (radial) strain gage goes around the circumference of the cylindrical sample (Figure 2.6). To apply the strain gage, a piece of scotch tape is laid out sticky side up on a clean lab bench. Using a clean pair of tweezers a new strain gage is removed from the package and carefully applied centered on the scotch tape with the matte side of the strain gage facing up. The entire tape-strain gage assembly is then picked up and placed on the copper foil wrapped around the sample so that the strain gage alignment tabs are aligned to the scribed marks on the copper foil. The tape allows for repositioning to ensure that the strain gage is properly aligned. Any misalignment of the gage induces errors in axial strain measurements. Once the strain gage is properly aligned the tape can be peeled back just enough so that the entire strain gage is lifted off of the copper foil but one edge of the tape is still stuck on the foil to retain the proper positioning of the strain gage. Cyanoacrylate glue made by micro-measurements (M bond 200) is used to permanently attach the gage to the copper foil. Two drops of the glue are placed on the strain gage, one at the leading edge of the gage closest to the portion of tape that is still stuck to the copper foil and the other in the middle of the gauge. The tape/gage are then re-applied to the sample using a squeegee action with a finger to ensure that there are no air bubbles under the strain gage, no excess glue under the strain gage, and ensuring that there is complete coverage of glue on the underside of the gage. At this point the gage is held in place with application of pressure using a forefinger or thumb on top of the gage, being sure that none of the glue has squeezed out and has the potential of gluing a finger to the

sample. The gage is held in place with slight finger pressure for about 2 minutes. At this point the glue has begun to set up and can be tested by starting to pull the tape back. The gage should be well adhered to the sample and should not pull away. Slowly pull the tape away from the gage/sample by pulling the tape parallel with the surface of the sample to prevent pulling the gage off of the sample. Once the tape is removed the same procedure is repeated for the radial strain gage. Once the second gage is attached, the sample is allowed to sit for a minimum of 2 hours to let the glue cure but overnight is best. Once the glue is cured leads are soldered to the strain gage, resistance recorded ensuring a solid and correct solder joint, and the sample column can then be assembled.



Figure 2.6: Cylindrical 2024 aluminum sample (2.54 cm in diameter) with axial and radial strain gages attached.

2.3.3 Strain Gage Conditioning

The working principle of strain gages is discussed early in this chapter. To convert the output voltage of the Wheatstone bridge circuit into a useful strain value, the circuit must be calibrated. One of the simpler ways to perform this calibration is to use a shunt resistor of known resistance into the Wheatstone bridge circuit to unbalance the bridge a known amount and observe the change in output voltage. The amplifier that was

used for the suite of deformation experiments was a Vishay 2100 series strain gage conditioner and amplifier system. This system comprises a factory installed $174.8 \text{ k}\Omega \pm 0.1\%$ resistor, which can be inserted into the bridge circuit via a toggle switch to simulate 1000 micro-strain at a gage factor of 2 (Measurement Group Inc., 1992). During the start and end of the experiment this resistor is inserted into the circuit via a toggle switch and the output voltage change is recorded, thus providing a conversion factor that a given change in voltage is equal to 1000 micro-strain and the strain change during the experiment can be converted from voltage to a useful strain value.

2.4 Calibration of Stress and Strain Measurements

The final calibration that is performed is to elastically deform a right cylinder of uniform material that has zero porosity and has been extensively studied before. The chosen material is 2024 Aluminum with known values; bulk modulus (K) of 78 GPa, Young's modulus (E) of 73 GPa, and Poisson ratio (ν) of 0.33 (Davis and Allen, 1990).

A calibration test was conducted on a 2024 aluminum cylindrical sample (25.4 mm in diameter and 50.8 mm in length) using the triaxial deformation apparatus. A confining pressure of 40 MPa was applied to the aluminum sample and the axial (ϵ_a) and radial (ϵ_r) strains are recorded (Figure 2.7a). Note that the convention for strain measurements is that shortening is positive whereas elongation is negative. It is shown that during hydrostatic loading ($\sigma_1 = \sigma_2 = \sigma_3$) the axial (ϵ_a) and radial (ϵ_r) of the aluminum sample shorten at comparable rate (isostatic compaction). The volumetric strain (e) can be calculated as $e = \epsilon_a + 2\epsilon_r$ (Figure 2.7b), where volume loss (compaction) is positive and volume increase (dilation) is negative. The bulk modulus $K = \Delta P / \Delta e = 87.5 \text{ GPa}$ is

determined, where the effective mean stress $P=(\sigma_1+\sigma_2+\sigma_3)/3$ (Figure 2.7b). The discrepancy between this measured value and the value of $K=78$ GPa for the bulk modulus from the literature (Davis and Allen, 1990), is believed to be due to work hardening of the sample during machining as well as the cyclic hydrostatic loading prior to deformation.

At confining pressure of 40MPa the radial stresses ($\sigma_2=\sigma_3$) were kept constant whereas the axial stress σ_1 was increased by advancing the main hydraulic ram at a constant displacement rate of 2.78×10^{-4} mm/s (1mm/hour), which corresponds to a strain rate of 5.5×10^{-6} s⁻¹ for a 50.8 mm long sample. The differential stress ($Q = \sigma_1 - \sigma_3$) as a function of axial strain is plotted in Figure 2.7c. The Young's modulus has been determined to be $E = \Delta Q / \Delta \epsilon_a = 76.6$ GPa. The Poisson ratio $\nu = -\epsilon_r / \epsilon_a$ has been determined to be 0.33 (Figure 2.7a). All of the measured elastic moduli, bulk modulus K , Young's modulus E , and Poisson ratio ν are in satisfactory agreements with published data (Davis and Allen, 1990), indicating that the strain gage and other sensors on the apparatus are working properly with acceptable precisions.

The goal of this study is to better understand faulting that occurs in the Earth's lithosphere because the quantitative knowledge of the mechanical processes involved in brittle faulting could aid in earthquake mitigation. At low confining pressures, a rock fails by dilatancy and brittle fracture when stressed beyond its elastic limit (e.g., Handin et al., 1963; Fredrich et al., 1989; Wong et al., 1997). This experimental study focuses on the effect of confining pressure and deviatoric stress on microcracking and the inelastic volume changes in porous rocks precede brittle faulting.

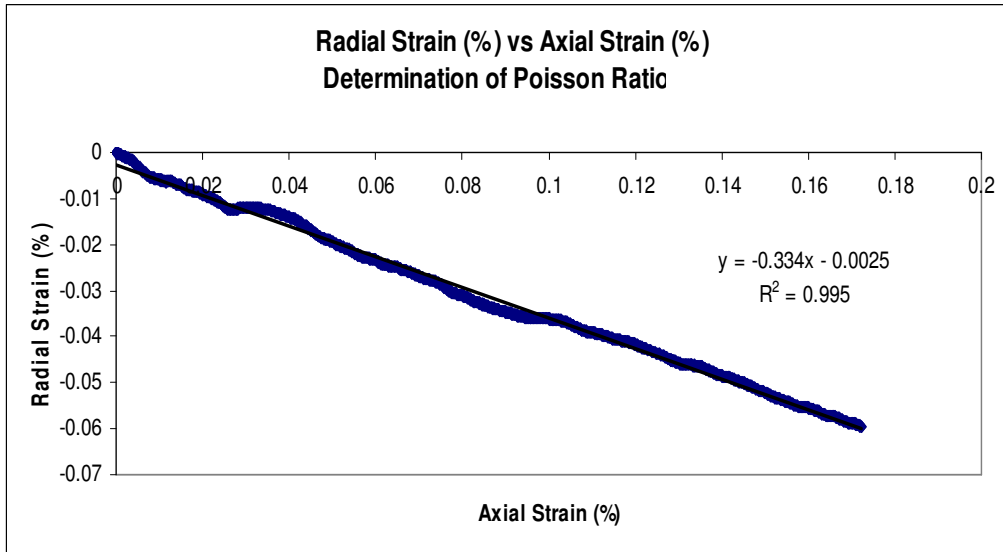


Figure 2.7a: Deformation of a 2024 aluminum sample: Poisson ratio 0.33 (confining pressure=40 MPa).

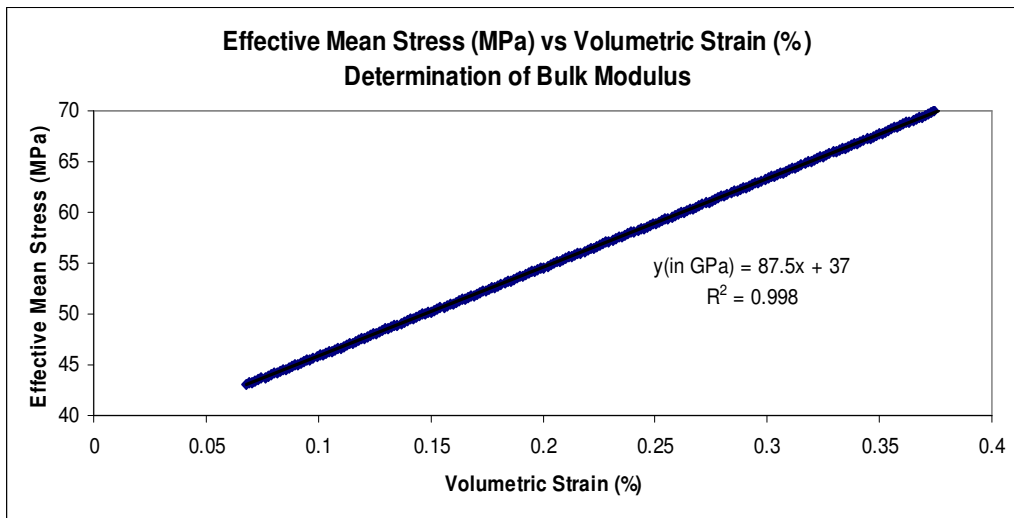


Figure 2.7b: Hydrostatic compaction of a 2024 aluminum sample: Bulk modulus 87.5 GPa.

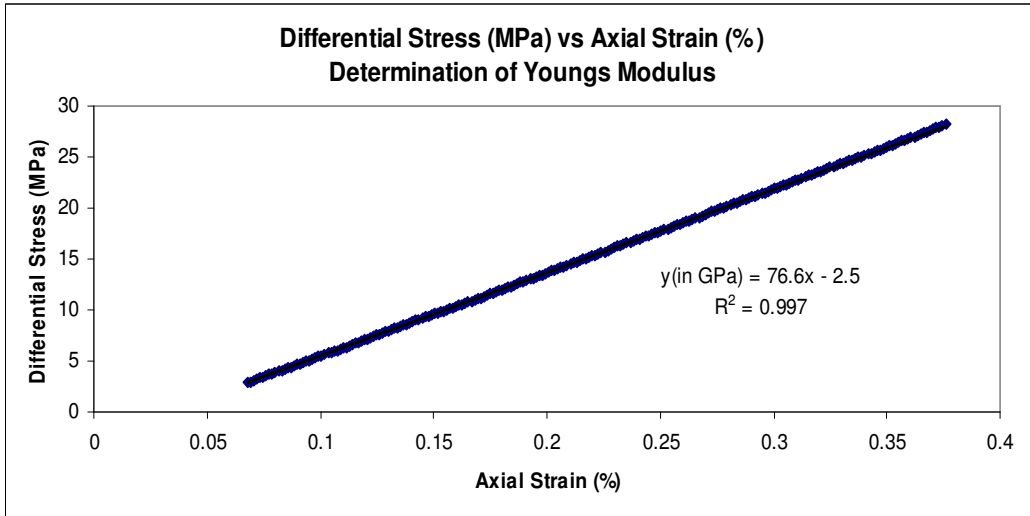


Figure 2.7c: Deformation of a 2024 aluminum sample: Young's modulus 76.6 GPa.

Chapter 3: Progressive Development of Brittle Faulting: Deformation Tests

Deformation experiments conducted under controlled conditions provide a useful tool to study the brittle failure phenomenon. The current understanding of brittle fracture generation in rocks is summarized in Figure 3.1. Using a simple classification, the stress-induced brittle deformation process can be divided into 5 stages (e.g., Wawersik and Brace, 1971, Scholz, 2002). The non-linear region (stage I) that is present at the initiation of stress application is due to crack closure caused by increasing effective pressure. The cracks of high aspect-ratio (i.e., ratio of crack length to its width) are more compliant (Walsh, 1965) and will be the first to close. At a certain stress level, most of the crack closure has occurred and the sample enters stage II, where the deformation is dominantly elastic (Brace et al., 1966). Ideally, the deformed sample could be unloaded at any point in this region and no permanent deformation or damage incurred. A further increase in stress results in growth of micro cracks within the sample, which defines the onset of irreversible plastic deformation of the sample. Stage III of the brittle deformation process is marked by the onset of dilatancy, an inelastic volume increase caused by stress induced microcrack growth, frictional sliding, and distortion of the grains (Brace et al., 1966). At high stress most rocks and granular aggregates dilate (Brace, 1978). The maximum stress that the sample can withstand is the brittle yield strength represented by stage IV. And finally in stage V, the development of macroscopic brittle failure is manifested by a stress drop associated with a yield softening material. Stage V is where microscopic damage coalesces into macroscopic fracture of

the sample. In porous materials the transition from fully brittle to fully plastic generally occurs over some range of pressure, temperature and strain rates (Brace 1978).

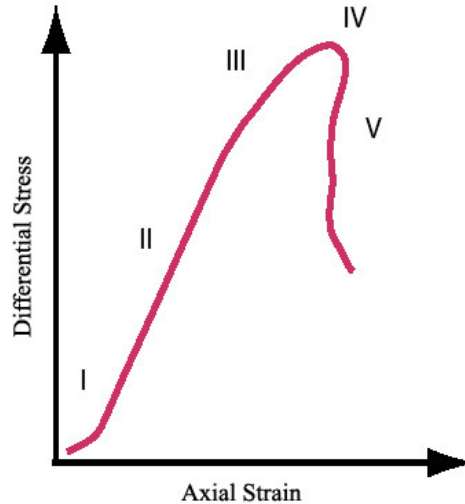


Figure 3.1: A typical differential stress- axial strain curve of a rock undergone brittle failure with the failure process divided into 5 different stages showing yield softening behavior (after Wawersik and Brace, 1971; Scholz, 2002).

The sample material used in this study is Darley Dale sandstone, carboniferous in age and quarried in England (Duff and Smith, 1992). Darley Dale sandstone is chosen because of its uniformity and reproducibility in mechanical behaviors (e.g., Wong et al., 1997; Baud et al., 2000; Heap et al., 2008). The grain size ranges from 0.08 to 0.8 mm in this poorly sorted quartz sandstone (Read et al. 1995), consisting of about 67% quartz, 14% feldspar, small amount of mica and siliceous and clay cement. The initial porosity of an intact sample is ~13% (e.g., Ismail, 1976).

3.1: Conventional Loading Path

In a conventional triaxial deformation test, a rock sample is first compressed hydrostatically ($\sigma_1=\sigma_2=\sigma_3=P_c$) to a desired effective pressure $P_0=P_c-P_f$, where constant pore fluid pressure (P_f) is maintained (i.e., fully drained condition). Subsequently,

deformation is achieved by keeping the radial stresses $\sigma_2=\sigma_3=P_c$, while advancing the axial piston at a constant strain rate through servo control (Figure 3.2). The mechanical behavior of Darley Dale sandstone deformed using the conventional triaxial compression loading shows the typical 5 stages failure process (Figure 3.3). The Young's modulus is determined to be 13.2 GPa. The reduction in compaction rate marks the onset of dilatancy (Figure 3.3b). Macroscopic shear fracture developed right after peak stress destroyed the strain gages, resulting in an abrupt stop in strain data recording (Figure 3.3b).

3.2: Lateral Relaxation Loading Path

To investigate the relationship between microscopic damage and macroscopic faulting, a new compressional loading configuration is adopted in this study. Under the new loading configuration, deformation is achieved by keeping the axial stress $\sigma_1= P_c$ constant while decreasing the radial stresses $\sigma_2=\sigma_3$ at a constant strain rate (Figure 3.2). In a conventional triaxial compression test, both the effective mean stress $P=(\sigma_1+\sigma_2+\sigma_3)/3-P_f$ and the differential stress $Q=(\sigma_1-\sigma_3)$ increase concomitantly during deformation. In contrast, the stress path of the new compression loading is such that the increase in differential stress Q is accompanied by a decrease in effective mean stress P (Figure 3.2). This so-called lateral relaxation loading configuration is shown to be an effective way to stabilize the post-yielding failure development thus allow the observation of changes that take place during faulting (Zhu et al., 2003).

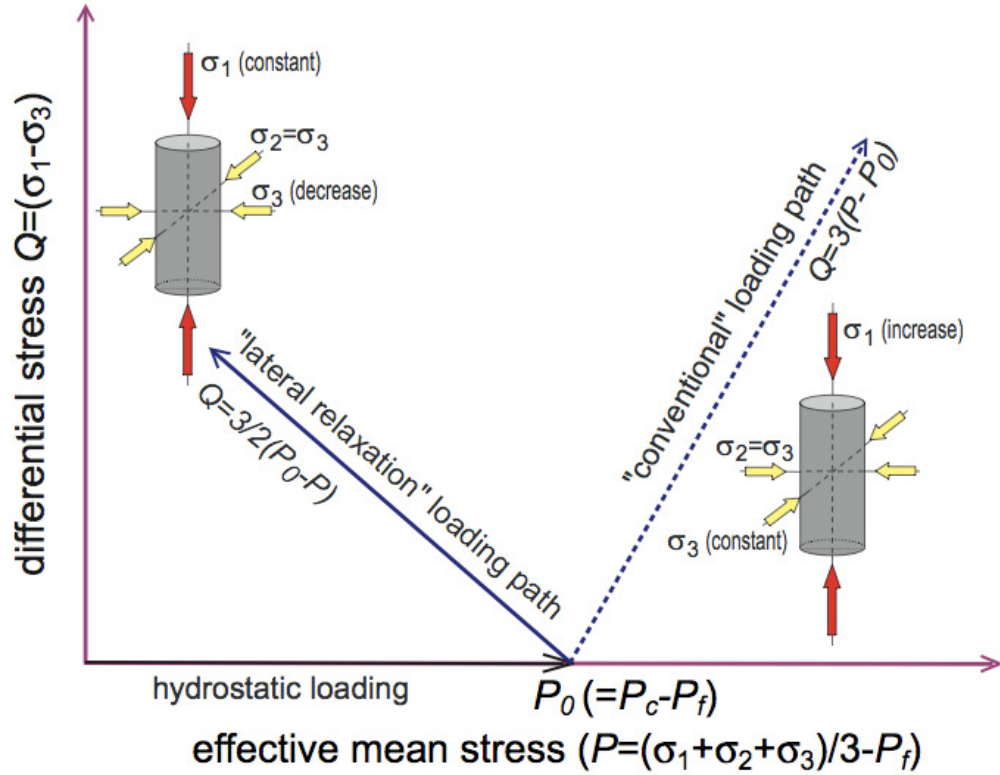


Figure 3.2: Comparison of a conventional loading path to that of the lateral relaxation loading path used in this study (after Zhu et al. 2003).

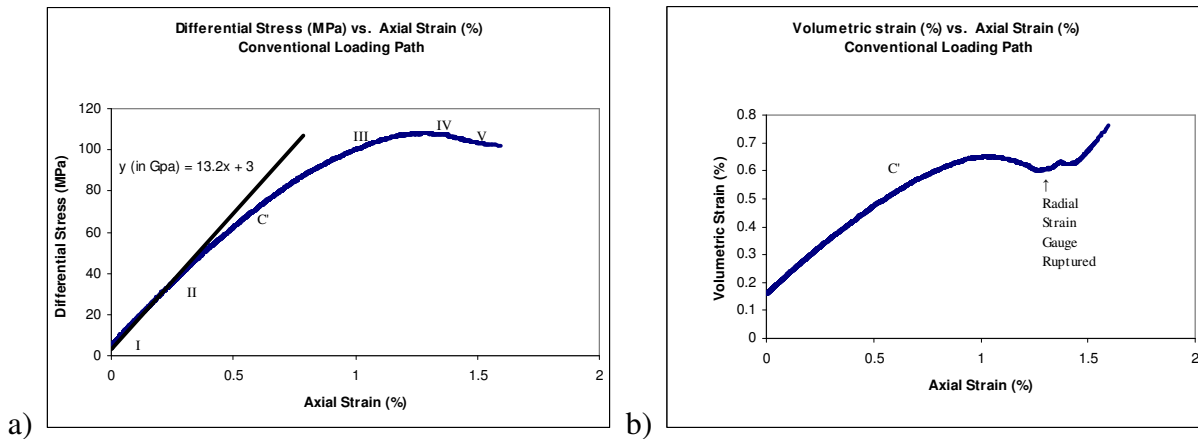
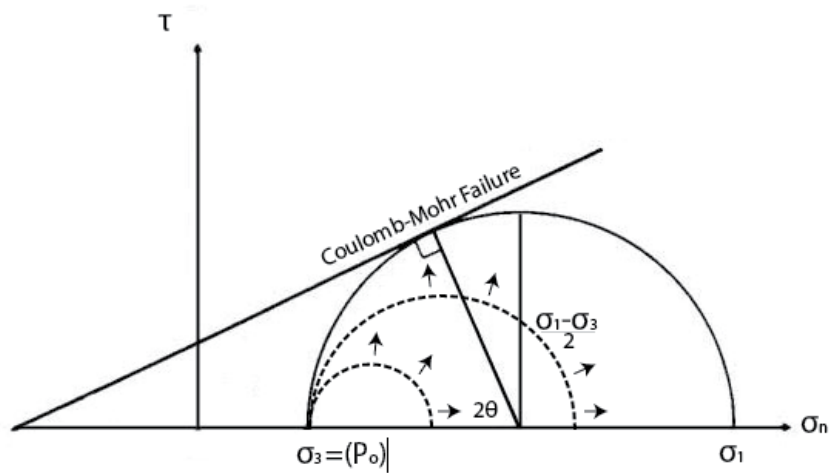


Figure 3.3: a) Stress-strain curve of a Darley Dale sandstone sample (dd-17) deformed at effective pressure of 70MPa using the conventional loading configuration. The 5 deformation stages are indicated; b) Volumetric strain as a function of axial strain during deformation. The onset of dilatancy is marked by the change in compaction rate (C'). Strain gages were destroyed by the shear fracture developed in stage V, shortly after sample reached its peak stress.

3.2.1: Mohr's Circle

a) conventional triaxial compression loading



b) lateral relaxation triaxial compressional loading

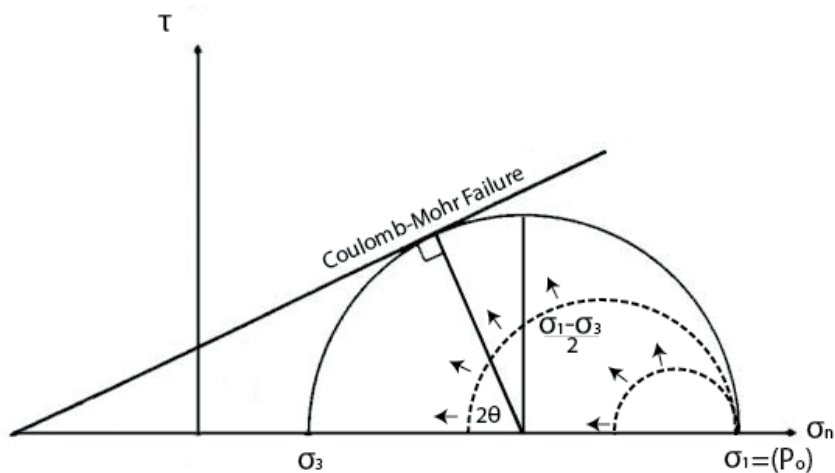


Figure 3.4: Stress states in a rock sample deformed a) under conventional triaxial compression loading; b) under lateral relaxation triaxial compressional loading, using Mohr's circle. The Coulomb-Mohr failure criterion is also shown. Dashed Mohr's circles represent intermediate stress state during deformation. Solid Mohr's circle represents the stress state at failure.

The difference between a conventional loading test and a lateral relaxation test is evident when the stress states are expressed using Mohr's circle. The Mohr's stress circle

is a graphical means of representing the shear stress (τ) and normal stress (σ_n) relationship. This relationship was discovered by Culmann (1866) and developed in detail by Mohr (1882), after whom the graphical method is now named. Combined with the Coulomb-Mohr brittle failure criterion, the Mohr's circle provides an excellent way to visualize the stress change as the sample approaches brittle fracture.

In Figure 3.4, the x-axis is the normal stress σ_n and the y-axis represents the shear stress τ . Due to the axisymmetric characteristics of the sample configuration (i.e., $\sigma_2 = \sigma_3$), the complete state of three dimensional stress is represented by all points on the circle. The center of the circle is at point $\sigma_0 = (\sigma_1 + \sigma_3)/2$ and $\tau=0$ where the principal stresses, σ_1 and σ_3 , are given by the points where the circle crosses the $\tau=0$ axis (Parry, 1995). For both the conventional and lateral relaxation loading experimental runs, the sample is initially loaded hydrostatically to a point of $\sigma_n = P_0$ and $\tau=0$. Following the conventional loading path (Figure 3.2), the radial stresses σ_2 and σ_3 are held constant at P_0 while the axial load is steadily increased. This results in the expansion of the Mohr's circle with its left side σ_3 fixed at P_0 . Failure occurs once the Mohr's circle intersects the Coulomb-Mohr failure envelope represented by the inclined line in Figure 3.4a. In a lateral relaxation test, following hydrostatic stress state of $\sigma_n = P_0$ and $\tau=0$, radial stresses σ_2 and σ_3 are gradually decreased while the axial stress σ_1 is held constant at P_0 . This loading configuration results in the expanding of the Mohr's circle with its right side σ_1 fixed at P_0 . Just as in a conventional test, failure occurs when the Mohr's circle eventually intercepts the failure envelope in Figure 3.4b.

Sample dd-05 was deformed at effective pressure of 190MPa under a nominal strain rate of $5.5 \times 10^{-6} \text{ s}^{-1}$ under the new lateral relaxation loading path. Comparison of

the mechanical data of dd-05 (relaxation loading path) dd-17 (conventional loading path) is shown in Figure 3.5. During deformation stages I-IV, as seen in Figure 3.5a, tests using different loading paths yield very similar Young's Modulus (slope of the linear portion of the stress-strain curve), yield stress (stress at the onset of dilatancy) and the brittle yield strength (i.e., peak stress). From the strain data, the Poisson ratio and the amount of dilatancy observed under different loading paths are also in good agreement. However, stage V deformation exhibits considerably larger gradual strain softening before shear fracture developed in samples deformed under the lateral relaxation loading (Figure 3.5). Using the new loading configuration, I am able to observe the gradual changes taken place before shear fracture is fully developed.

3.3: Strain Rates

A total of 6 successful experiments were performed at 3 different strain rates; $1.8 \times 10^{-6} \text{ s}^{-1}$, $2.5 \times 10^{-6} \text{ s}^{-1}$ and $5.5 \times 10^{-6} \text{ s}^{-1}$ (Table 3.1). All of the experiments are conducted at an effective pressure $P_0=190\text{MPa}$, with a constant pore pressure of 10MPa maintained during deformation. Once the P_0 reaches its desired value, the confining pressure (σ_2 and σ_3) is decreased at a constant rate of 3.6 MPa/s . Samples dd-05, dd-08 and dd-10 were deformed at a constant axial stress σ_1 , with the main hydraulic ram advancing at a constant displacement rate of $\sim 4 \times 10^{-4} \text{ mm/s}$, which corresponds to a nominal axial strain rate of $5.5 \times 10^{-6} \text{ s}^{-1}$ (Figure 3.6).

In a lateral relaxation test, the effective mean stress steadily decreases (moves to the left in Figure 3.4b), while the differential stress increases. After the sample reaches its brittle yield strength (the peak stress), the shear localization begins to develop (Stage V).

As the failure slowly progresses the differential stress decreases as well as the confining pressure and therefore effective mean stress, until the experiment is stopped.

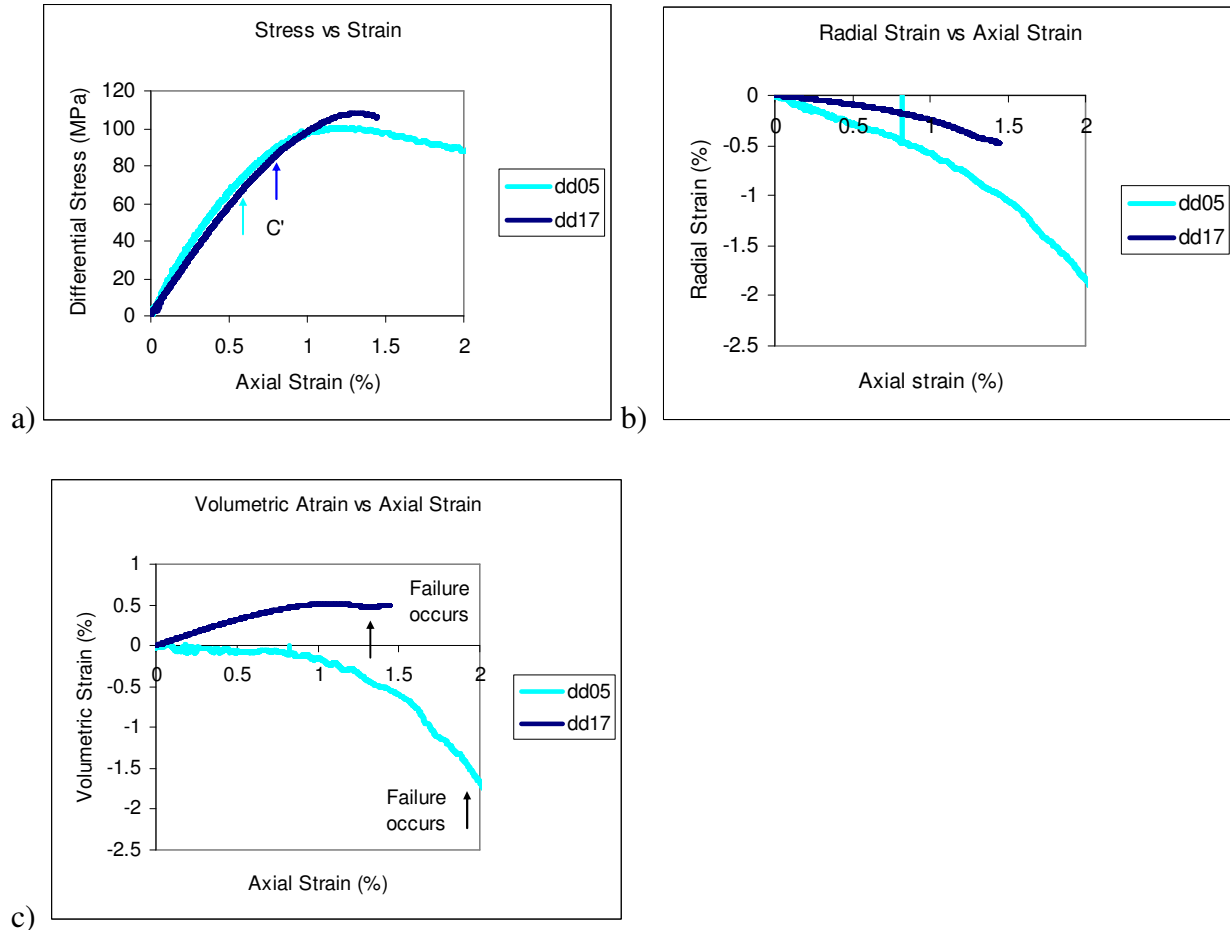


Figure 3.5: Comparison of the mechanical data between sample dd-05 deformed under the lateral relaxation loading configuration (at effective pressure $P_0=190$ MPa) and sample dd-17 deformed under the conventional loading configuration (at $P_0=70$ MPa). a) stress-strain curve; b) radial strain vs. axial strain; c) volumetric strain vs. axial strain.

The axial strain is plotted in Figure 3.6b against time. As can be seen the strain is initially linear and then changes slope where the sample starts to become dilatant. The volumetric strain versus axial strain is plotted in Figure 3.6c. The onset of dilatancy marks the transition from dominantly elastic deformation to inelastic deformation.

Sample dd-10 was unloaded just beyond its peak strength (Figure 3.6a). While dilatancy and strain softening are observed in both dd-08 and dd-10, visual examination of deformed samples reveal an obvious shear fracture in dd-08 (Figure 3.7) and no visible shear fracture is detected in dd-10.

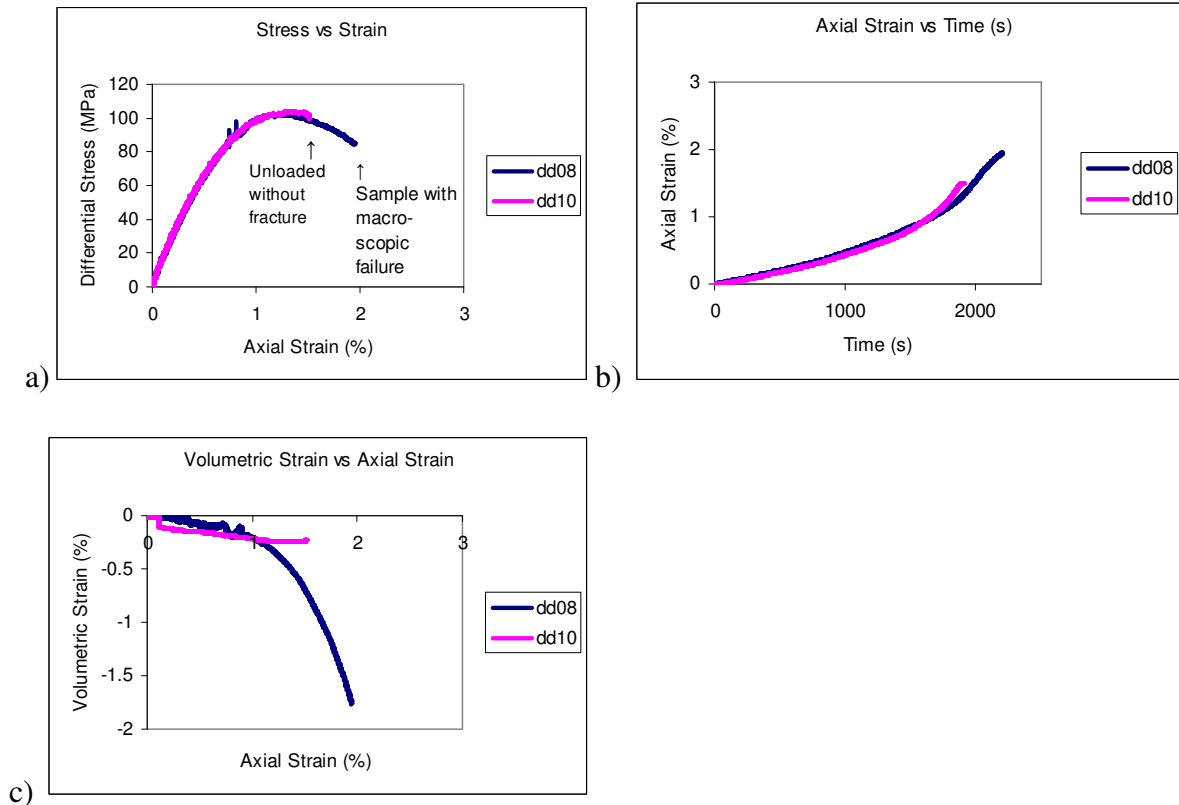


Figure 3.6: Comparison of mechanical data of dd-08 and dd-10, deformed at a strain rate of $5.5 \times 10^{-6} \text{ s}^{-1}$. Sample dd-08 underwent considerable strain softening and a macroscopic shear fracture is developed, whereas sample dd-10 was unloaded shortly after reaching the peak stress, no macroscopic shear fracture is observed. a) stress strain curve; b) axial strain over time; c) volumetric strain vs. axial strain.

Sample dd-06 and dd-09 were conducted using a slower main hydraulic ram advancement rate $2 \times 10^{-4} \text{ mm/s}$, which corresponds to a nominal axial strain rate of $2.5 \times 10^{-6} \text{ /s}$. For sample dd-04, the main hydraulic ram was locked, rendering the slowest

strain rate of 1.8×10^{-6} /s. Given the same confining pressure release rate of 3.6 MPa/s in all 6 tests, the axial stress σ_1 in deformation tests on dd-04, dd-06, and dd-09 was not kept constant during deformation.

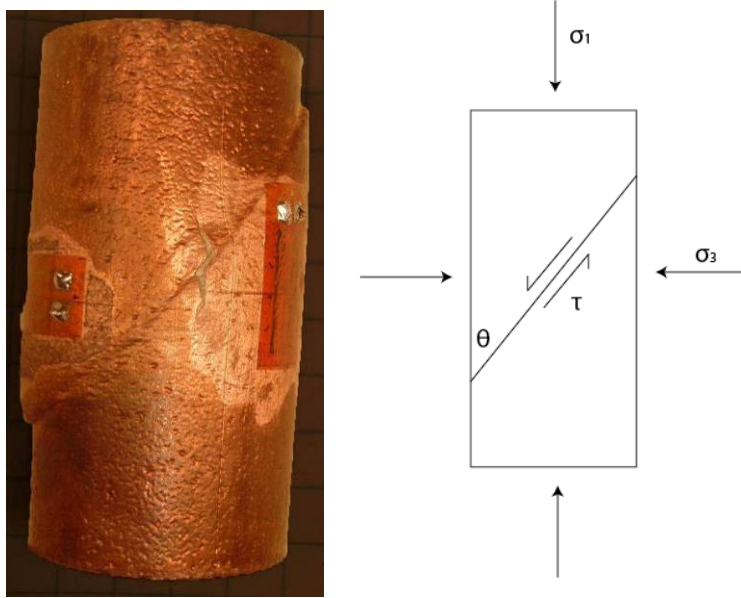


Figure 3.7: a) Post failure sample (dd-08) with obvious shear localization and b) schematic diagram showing the relations between the orientation of shear fracture plane and the principal stress directions.

The effect of strain rate on brittle deformation is observed (Figure 3.8). Mechanical data of samples dd-05 and dd-06, deformed at 2 different strain rates, $2.5 \times 10^{-6} \text{ s}^{-1}$ and $5.5 \times 10^{-6} \text{ s}^{-1}$, respectively, are shown in Fig. 3.8. Sample dd-05 deformed at a higher strain rate, reaches a higher yield stress and peak stress, compared to sample dd-06. However, the amount of dilatancy is comparable (Figure 3.8)

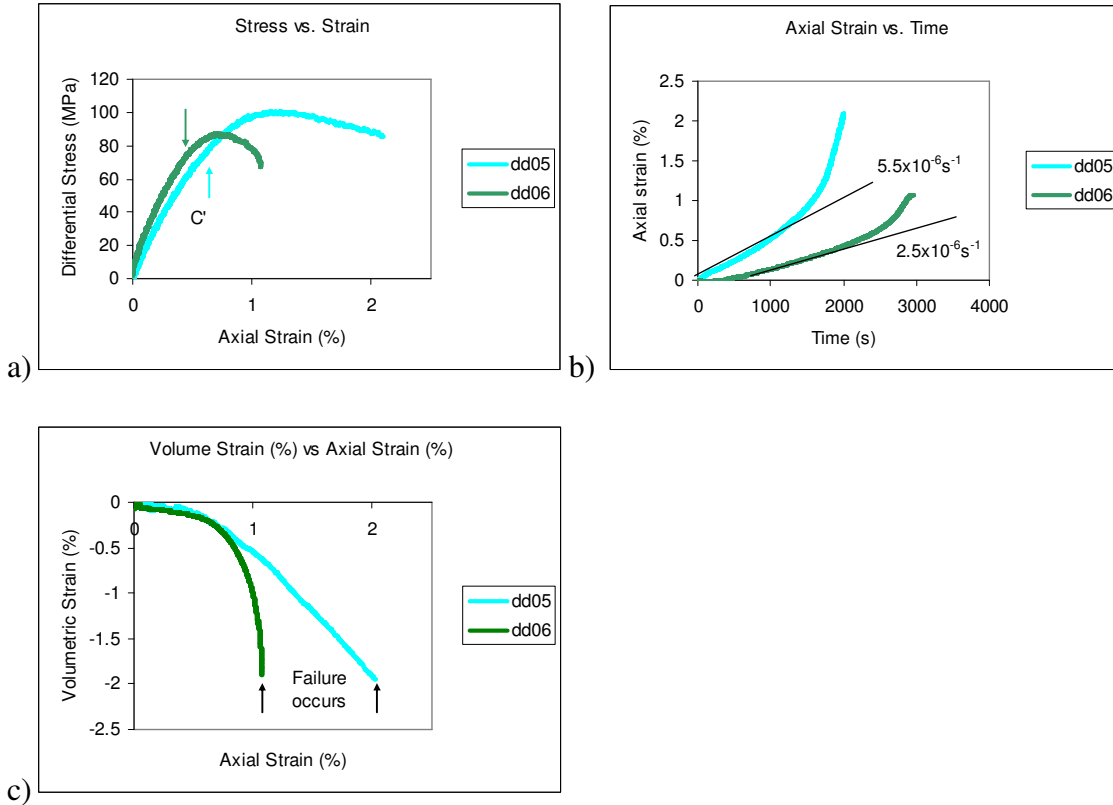


Figure 3.8: Mechanical data from sample dd-05 (strain rate of $5.5 \times 10^{-6} \text{ s}^{-1}$) and dd-06 (strain rate of $2.5 \times 10^{-6} \text{ s}^{-1}$) a) stress-strain curve; b) axial strain over time c) volumetric strain vs. axial strain.

3.4: Faulting Energy

When a shear fracture is developed presenting the deformed sample (Figure 3.7), the angle of failure can be directly measured (Table 3.1). Using the strain data, the amount of slip occurring along the macroscopic fracture can be derived (Wong 1982):

$$\Delta u = \Delta l / \cos(\theta)$$

Furthermore, shear and normal stresses along the fracture can also be calculated (Wong 1982):

$$\tau = ((\sigma_1 - \sigma_3) / 2) \sin(2\theta)$$

Since strain data was monitored continuously during the experiment we can back out the change in length of the sample due to faulting and then divided by the cosine of

the failure angle to determine the slip that has occurred along the fault. The plot of the shear stress vs. fault slip is shown in Figure 3.9. The area under this curve is the calculated fracture energy.

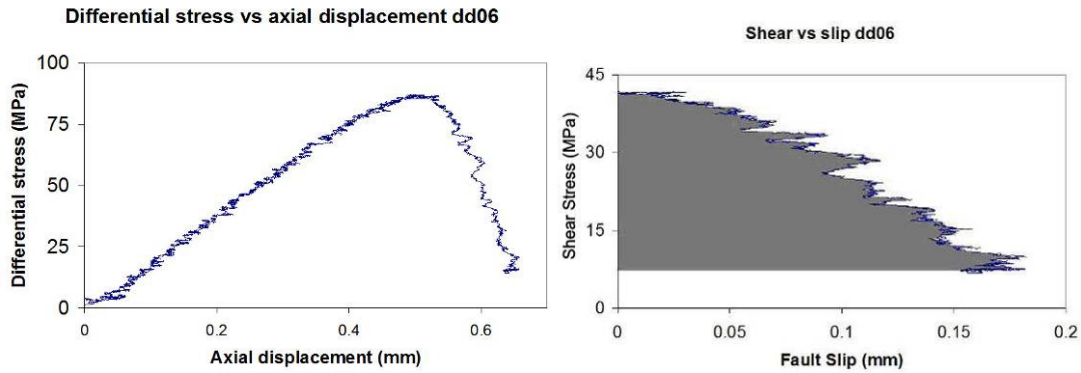


Figure 3.9: Transformation of a) experimental deformation data to infer b) the shear stress verses relative fault slip allowing the fracture energy to be measured as the area under the shear vs. fault slip curve.

	dd-04	dd-05	dd-06	dd-08	dd-09	dd-10	dd-17
strain rate (s^{-1})	1.8×10^{-6}	5.5×10^{-6}	2.5×10^{-6}	5.5×10^{-6}	2.5×10^{-6}	5.5×10^{-6}	5.5×10^{-6}
brittle strength (MPa)	76.5	100.3	86.9	102.6	86.0	103.2	107
Young's modulus E (GPa)	15.9	12.9	14.6	12.9	15.7	12.9	13.2
fracture energy (Jm^{-2})	5100	14100	3100	12900	n/a	n/a	4700
fracture angle ($^{\circ}$)	37.9	36.9	37.1	38.6	n/a	n/a	39.8

Table 3.1: Experimental results from lateral relaxation loading of Darley Dale sandstone at two different strain rates. dd-09 and dd-10 were removed prior to macroscopic fault development and dd-17 is the only sample run using the conventional loading path.

The results from all of the experimental runs are shown in table 2. The fracture energy ranges from $3100 J/m^2$ to $14100 J/m^2$. These results are comparable to the fracture energy of other experiments using a conventional loading path (Wong, 1982) and these results fit well with the empirical envelopes that have been shown to be applicable to other porous sandstones (Klein et al.2001, Baud et al. 2000 and Wong et al. 1997).

This confirms that the lateral relaxation loading path is an effective technique to study the onset and propagation of brittle failure.

The effective pressure controls the deformation of rocks based on changes in confining pressure and pore pressure. The conventional loading path uses an increase in axial load (σ_1) while maintaining a constant confining pressure (σ_2 and σ_3). Since failure occurs so quickly with conventional loading, the inelastic behavior and failure mode have been difficult to investigate. The lateral relaxation loading path allows the failure to be slowed down so that the details of the failure process can be observed. Since the lateral relaxation loading path fracture energy is comparable to the conventional loading path, the slower energy release rate will be useful to investigate the inelastic behavior of failure.

Chapter 4: Progressive Development of Brittle Faulting: Microstructural Analysis

The precursory phenomena such as volatile release from crustal rocks and magnetic and electric field perturbations have been studied for earthquake prediction (Brace and Orange, 1968; Scholz et al. 1973; King, 1986; Park, 1991; Fenoglio, 1995; Johnston, 1997). Precursory phenomena are generally linked to crack opening in fault rocks during interseismic strain accumulation in an active tectonic environment (e.g., Reid, 1910; Scholz, 2002).

It is known that dilatancy, caused by changes in packing of the grains and the generation of micro cracks within the grains (Patterson and Wong, 2005), precedes macroscopic fracture development in rocks during brittle failure (e.g., Brace et al., 1966; Wong, 1982; Lockner et al., 1992; Menéndez et al. 1996). Slip at grain contact and intergranular microcracking can generate high frequency (from kHz to hundreds of MHz) acoustic events (e.g., Lockner et al., 1992). Locating the acoustic emission activity during deformation, Lockner et al. (1992) showed that at deformation stages I to III the stress-induced microstructural damage is randomly distributed, with the locations likely dictated by the pre-existing defects. Beyond stage IV, microstructural damage becomes localized to form a macroscopic fracture (Figure 4.1 A-E). During stage V, the nascent fault continues to grow and steepen which leads to a shear fracture at an acute angle across the sample (Figure 4.1 D-E).

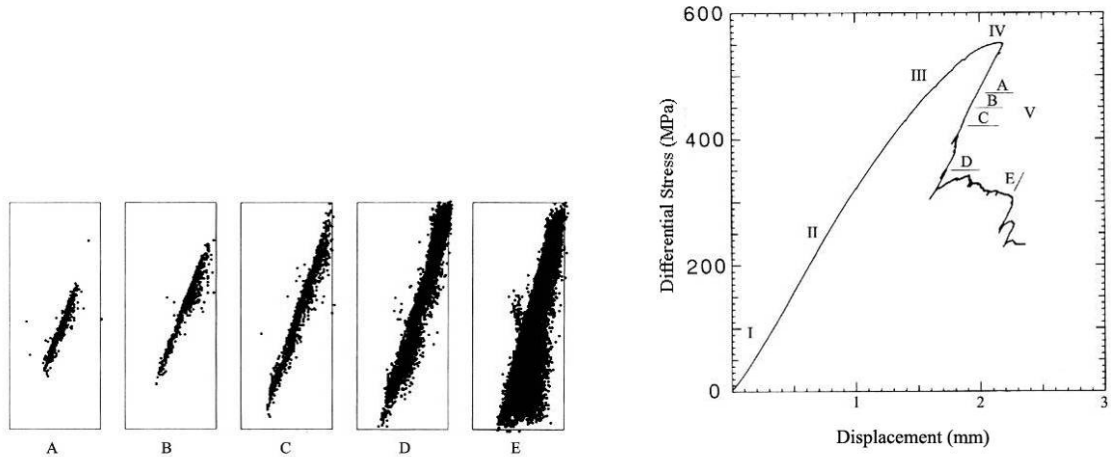


Figure 4.1: Plots of acoustic emissions during shear localization of sample (Lockner et al. 1992)

However, acoustic emission activity probably accounts for less than 10% of actual microstructural damage occurred during deformation (Lockner et al., 1992). Quantitative understanding of fault growth requires systematic microstructural analysis on deformed samples. To better understand the relationship between dilatancy, microcracking and fault initiation and propagation, we have conducted a quantitative microstructural analysis on post-failure Darley Dale sandstones samples, at various stages of macroscopic faulting development.

Samples from two different suites of experiments were used for microstructural analysis. The first suite, the DDL series, consists of 4 samples. These four samples were deformed using the triaxial deformation apparatus in the rock mechanics lab at the Stony Brook University. The loading path is identical to the experiments described in Chapter 3. The DDL samples were deformed at a constant nominal strain rate of $\sim 5 \times 10^{-5}$ /s. Sample DDL45 was deformed at an effective pressure of 80 MPa (with distilled water as pore fluid at $P_f=10$ MPa). Sample DDL46 was deformed at an effective pressure of 150

MPa (with $P_f=10\text{MPa}$). Samples DDL47 and DDL49 were both deformed at the same effective pressure of 200 MPa (with $P_f=10\text{MPa}$). The difference between DDL47 and DDL49 is that DDL47 was unloaded (i.e., release of axial stress and confining pressure) at a higher stress level (before the stress drop associated with faulting was completed) compared to DDL49. The second suite of samples, the dd series, were deformed using the triaxial deformation apparatus in the rock physics lab at the University of Maryland. All of the experiments were conducted at a constant effective pressure of 190MPa (with $P_f=10\text{MPa}$) with various strain rates, ranging from $1.8 \times 10^{-6} \text{ s}^{-1}$ and $5.5 \times 10^{-6} \text{ s}^{-1}$. Detailed description of the loading configuration, experimental procedure and elastic and inelastic behaviors of the samples can be found in Chapter 3.

4.1 Characterization of Microscopic Damage: Damage Index

Reflected light images of the four DDL thin sections made from the deformed samples are shown in Figure 4.2. While the mechanical data indicate that all 4 samples have undergone dilatancy and strain softening during deformation (Zhu et al., 2003), no macroscopic shear fracture is observed in DDL45, but a shear fracture can be clearly identified in DDL46 and DDL49, respectively. Compared to DDL49, the macroscopic shear fracture in DDL47 is not as pronounced. While these samples are deformed at comparable strain rate, DDL45 was deformed at the lowest effective pressure of 80 MPa. Samples DDL47 and DDL49 were deformed under identical conditions (Figure 4.3), however, DDL47 was unloaded before the post-yield stress drop was completed. The contrast between DDL47 and DDL49 provides further evidence that the post-yielding deformation under the new loading configuration is stable enough to allow detailed investigation of brittle fracture process.

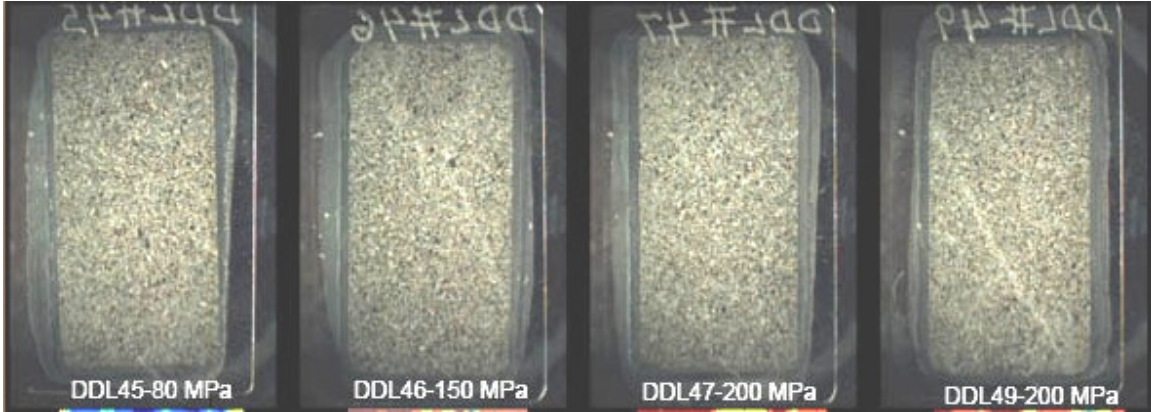


Figure 4.2: A reflected light image of the four DDL thin sections. Corresponding effective pressure used in the deformation test for that sample is indicated next to sample label. Nominal strain rate is $\sim 5 \times 10^{-5}$ /s.

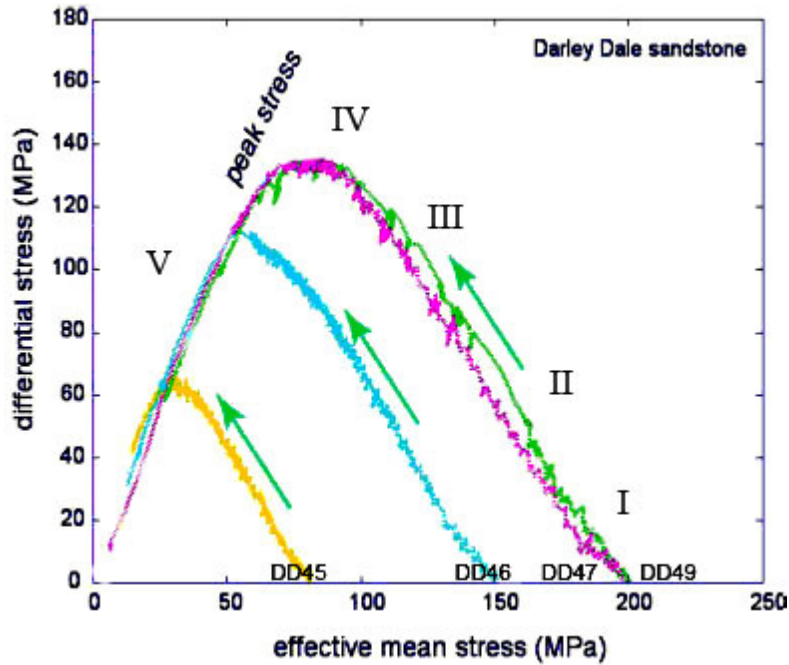


Figure 4.3: Loading paths for DDL45, DDL46, DDL47 and DDL49. Deformation stages I-V (see Figure 3.1) are indicated (After Zhu et al. 2003).

To analyze the damage present in each sample, we followed a damage index developed by Menéndez et al.(1996), shown in Figure 4.4. An index value of zero represents a grain with no damage. Increasing in index values from 1 to 4 indicates higher

intergranular micro crack density. An index value of 1 represents grains with 1 visible micro crack. At the maximum value of 4, 4 or more micro cracks can be seen within a grain.

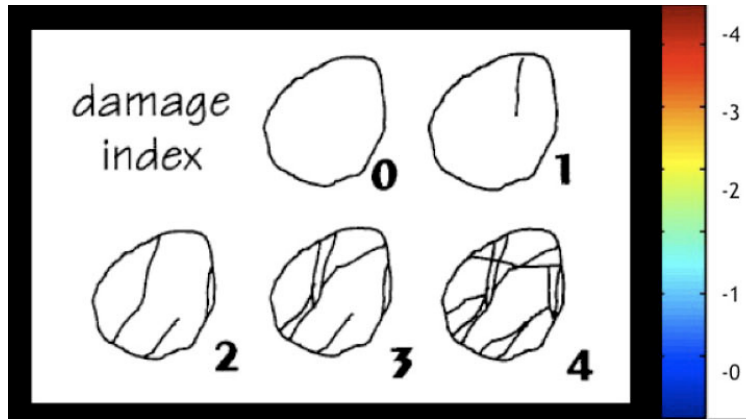


Figure 4.4: Damage index developed by Menéndez et al.(1996) and associated color scheme used.

We assigned each of these index numbers to a specific color value and these colors were then plotted to give a damage map of the thin section (Figure 4.5). The blue regions represent areas of minimum damage, damage index of zero, and red regions indicate areas of maximum grain damage, a damage index of 4 (Tamarkin and Zhu, 2009). Damage index analyses were performed over the entire thin section for each sample (Figures 4.5a). For reference, damage index map of an undeformed sample dd-00 is also shown (Figure 4.5b).

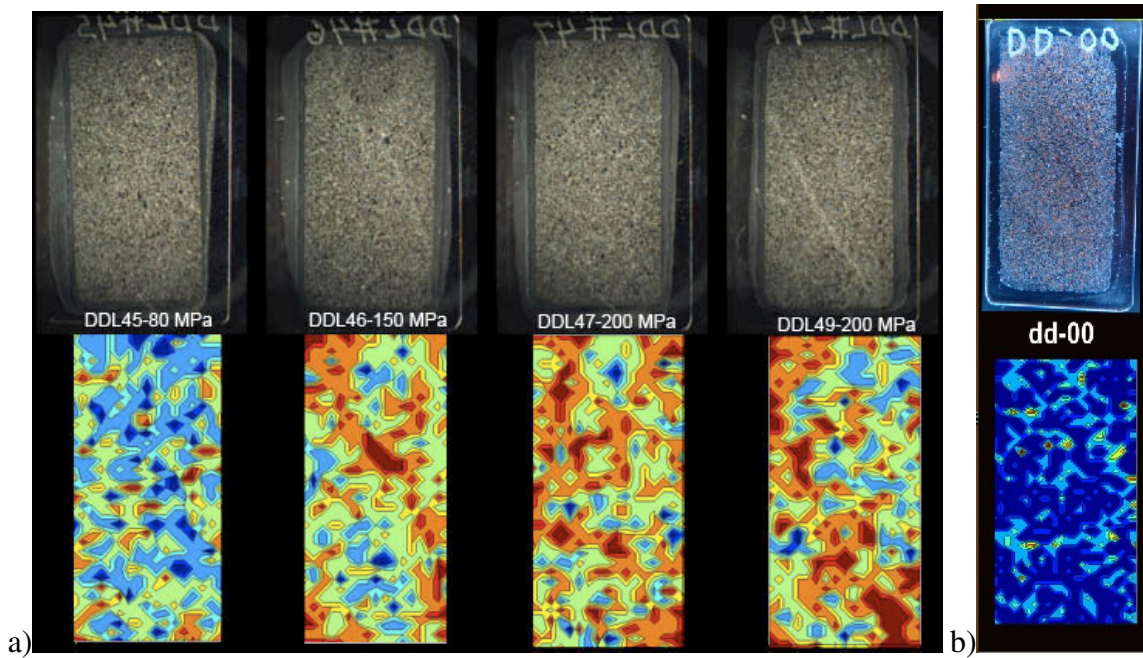


Figure 4.5a: Reflected light image of the 4 experimental DDL runs with corresponding damage index all 4 DDL samples have a 1.84 cm (0.725 inch) diameter (shorter dimension of thin section). b) Reflected light image of dd-00 the undeformed control with 2.54 cm (1 inch) diameter (shorter dimension of thin section).

The macroscopic fractures observed in samples DDL46 and DDL49 under reflected light are well represented in the damaged index analyses of the thin sections, with the highest crack density (damage index of 4) located within the shear fractures. In comparison, sample DDL47, shows no obvious shear fracture in the reflected light image and also shows intense red regions with a damage index of 4. The damage index indicates that there is a similar amount of damage incurred by the grains of DDL47 and DDL49 (Figure 4.5), however, the high crack density regions in DDL47 spread considerably wider so that the shear band is not as steep as in DDL49. Samples DDL47 and DDL 49 were deformed at the same strain rate and under the same effective pressure, with DDL47 unloaded at earlier stage during the fault propagation. The damage index analysis confirms that microscopic damage becomes progressively more correlated at

stage V, in agreement with the steepening trend of acoustic emission observed by Lockner et al. (1992) (Figure 4.1).

Sample DDL45 has the lowest damage index and no clear localized deformation zone is identified. While deformation stages I-IV are similar in all DDL samples, the stage V deformation in DDL45 is much limited compared to the other 3 DDL samples, due to the restriction of the low effective pressure (Figure 4.3). This observation provides further evidence that shear fracture develops during stage V. The lack of macroscopic fracture in DDL45 implies that a critical amount of post-yielding deformation must be attained before shear fracture propagates.

4.2 Quantification of Microcrack Density

To further investigate the relationship between the extent of microscopic damage and the development of macroscopic fracture, I conducted new deformation tests on Darley Dale sandstone samples. A total of six more samples were deformed at an effective pressure of 190 MPa. Based on results from DDL series, it is clear that comparison of samples with different degrees of post-failure deformation provides important information on the links between progressive microscopic damage and macroscopic fracture development. Two approaches were used to achieve different degrees of post-failure deformation in different samples. First, different strain rates were used so that different yield stresses were achieved (Figure 4.6). Second, for a fixed strain rate, deformation of samples was stopped at different post-yielding stress levels during stage V (Figure 4.6). A reflected light image of the six thin sections made from the deformed samples (dd-04, dd-05, dd-06, dd-08, dd-09, and dd-10) show varying degrees

of microstructural and macrostructural damage (Figure 4.7). Again, the undeformed sample dd-00 is shown as a reference.

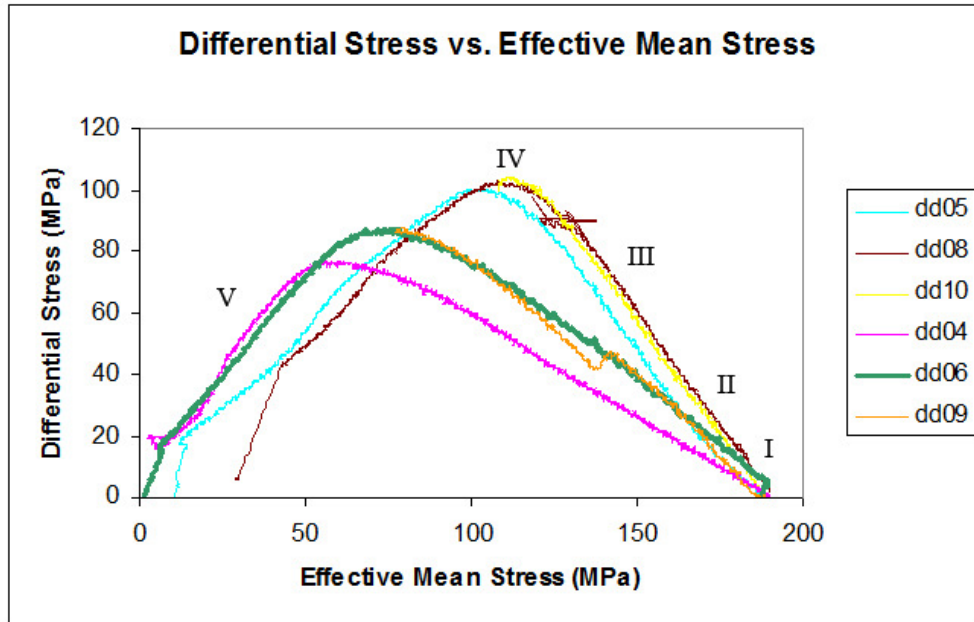


Figure 4.6: Loading paths for dd-04, dd-05, dd-06, dd-08, dd-09, and dd-10. Deformation stages I-V (see Figure 3.1) are indicated.

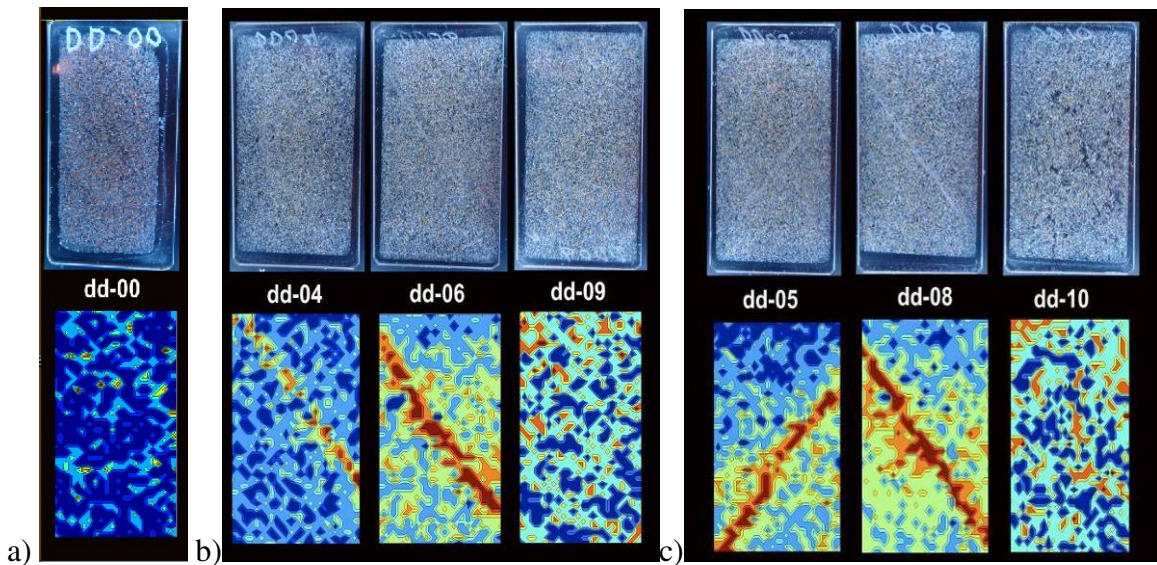


Figure 4.7: Reflected light image of the 6 experimental runs a) dd-00 undeformed control b) dd-04 run at a strain rate of $1.8 \times 10^{-6} \text{ s}^{-1}$; dd-06, and dd-09 run at a strain rate of $2.5 \times 10^{-6} \text{ s}^{-1}$ and c) dd-05, dd-08, and dd-10 run at a strain rate of $5.5 \times 10^{-6} \text{ s}^{-1}$ with corresponding damage index. All samples have a 2.54 cm (1 inch) diameter (shorter dimension of thin section)

The suite of experiments was run at two different strain rates as indicated in Figure 4.7. Sample dd-04 was run at a strain rate of $1.8 \times 10^{-6} \text{ s}^{-1}$, dd-06 and dd-09 were run at a strain rate of $2.5 \times 10^{-6} \text{ s}^{-1}$ while dd-05, dd-08 and dd-10 were all run at a strain rate of $5.5 \times 10^{-6} \text{ s}^{-1}$. Sample dd-09 shows a zig zag in the first stages of sample loading. This is a result of a piece of the viton jacketing material being caught between the sample and end cap. This change in strain rate is the point at which the viton yields plastically. As soon as the small piece of viton has completely yielded (extrudes from under the sample) the loading returns to the desired strain rate. Within each strain rate two of the samples were allowed to fail completely (dd-04 for a strain rate of $1.8 \times 10^{-6} \text{ s}^{-1}$ and dd-06 for a strain rate of $2.5 \times 10^{-6} \text{ s}^{-1}$ as well as dd-05 and dd-08 for a strain rate of $5.5 \times 10^{-6} \text{ s}^{-1}$). The final two samples, dd-09 ($2.5 \times 10^{-6} \text{ s}^{-1}$) and dd-10 ($5.5 \times 10^{-6} \text{ s}^{-1}$), were stopped at a maximum differential stress, just before the initiation of failure. This allows for the microstructural analysis of the samples just prior to the onset of macroscopic failure and allows this information to be compared to the undeformed sample dd-00 and the other deformed samples.

To further quantify the amount of damage present in each one of these samples, a crack density analysis, developed by Tamarkin and Zhu (2009), was performed. To do this, a high-resolution image of the thin section was obtained via stitching together many individual reflected light images taken through a microscope and a matlab code was developed and used to analyze the image. To perform the image analysis, a 2000 pixel diameter area of the thin section was analyzed independently from the rest of the image, Figure 4.8. A circular image was used for the simple reason that it was symmetrical and

had the same number of pixels independent of the angle of examination as long as this examination took place along a line that passes through the center of the circular image. A diameter of 2000 pixels was chosen to optimize the locations that could be analyzed in the image of the thin section. The dimensions of the entire thin section image were approximately 5050 x 10500 pixels or 1.84 cm x 3.81 cm (0.725 inches x 1.5 inches) for the DDL samples, and approximately 7000 x 11000 pixels or 2.54cm x 4.06 (1 inch x 1.6 inches) for the dd samples. The original 2.54 cm x 5.08 cm (1 inch x 2 inches) dd samples were trimmed by the company that made the thin sections to ensure the sample fit on the glass slide. The portion of the sample opposite the failure (Figure 4.9) was chosen to be removed to minimize loss of important areas of grain failure. Although this procedure was not requested, there was no apparent loss of information by this action. An additional feature of using an examination size of 2000 pixels was that this examination size allowed investigation of the corners of the image without losing part of the image or unwanted incorporation of material from the center of the image.

The circular image of the region of interest, chosen based on the areas of maximum and minimum damage as indicated by the damage index, was placed on a square black background of 2000 x 2000 pixels and Matlab was used to convert this image to a binary array where black pixels represent “0”s and white pixels represent “1”s (See appendix for the Matlab code that was used). The amount of damage in that region of interest is determined with the aid of a second image composed of a single, one pixel width, white line at the angle of interest on a square black background that has a size of 2000x2000 pixels. These two images (the same size) image were then converted to a binary array, the same way that the image of the thin section was, and then these two

arrays were summed. Whenever the white line (“1”s) would overlap with a grain (grains are white and therefore ones as well) it would sum to “2” and the rest of the array remained “0”s and “1”s. A simple count of the number of “2”s in the newly created array would give a value as to the area of grains that were present along that line of a given angle. This analysis was performed for all angles at 5° increments and indicated the grain area along these angles can then be examined and compared.

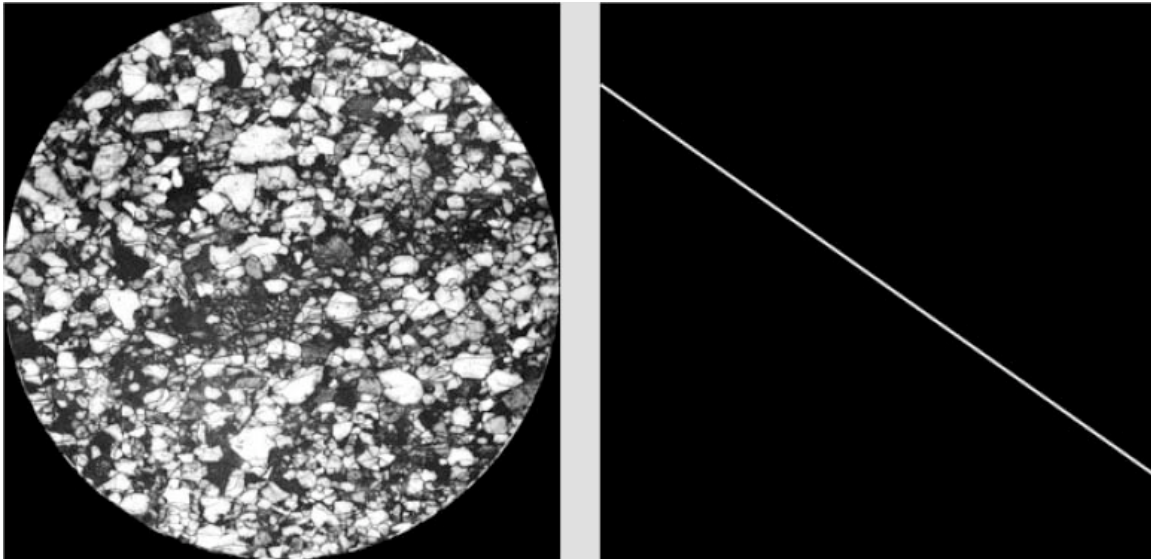


Figure 4.8: Crack density analysis and image binarization. Black pixels are converted to binary “1”s and white to “0”s. Sum array is made from circular image and white line at a desired angle of investigation. Then search for the number of “2”s in the newly created array.

Since a 1-pixel width line in a 2000 x 2000 array will have 2000 pixels in it, independent of the angle that it is positioned at, the count had to be normalized to compensate for the decreased area analyzed for angles not equal to 0° or 90°. This normalization was based the projection of the pixel count magnitude onto the ratio of the

side of the triangle that lies along the arbitrary horizontal axis to the length of the hypotenuse. Validation of this normalization technique is provided in the appendix.

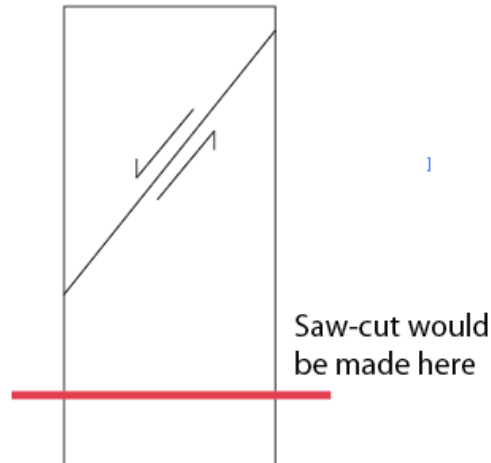


Figure 4.9: Example of location where samples were trimmed by the thin section company. None of the areas with obvious failures were trimmed away.

To further quantify the damage of each sample, the number of grains present would need to be known. To do this, the feature boundaries of the grains (grain edges and fractures) were identified using the built in Matlab function “edgeimage” as shown in Figure 4.10. By analyzing the feature boundaries of the same 2000 diameter pixel area analyzed for grain area, a new array was made, composing the outline of all of the feature boundaries. The same technique of summing this array with the 1 pixel width line at a given angle was performed. The resulting feature boundary analysis was used in conjunction with the grain area analysis to calculate the crack density along a given angle. Since the grain area encountered by each of these lines is known, and the number of feature boundaries encountered is known, an assessment of the estimated number of cracks per grain could be made by dividing the feature boundary count by the grain area

along a given angle and then multiplying by an average grain size. The average grain size was determined via point counting to be 0.17 ± 0.01 mm (Error based on Poisson counting statistics). The results of these calculations are shown in Figure 4.11.

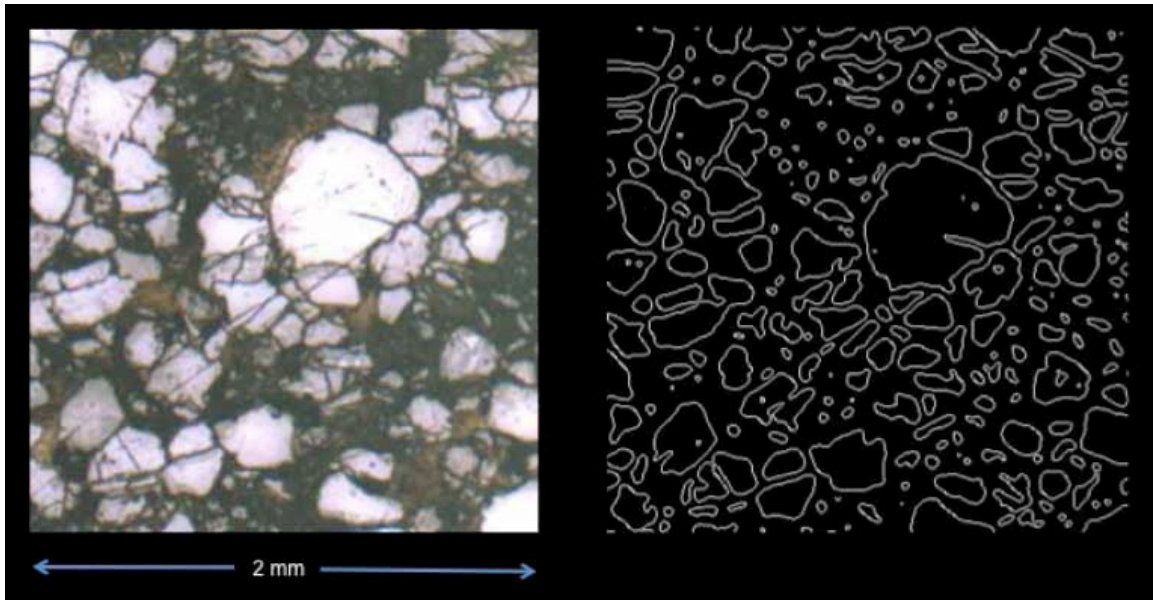


Figure 4.10: Matlab function “edgeimage” identifies the edges of grains and cracks within the grains.

The analyses were performed on both the most and the least damaged areas of the thin sections as indicated by the damage index. The areas of maximum damage were analyzed at all angles and the maximum crack densities of all of these values were plotted in Figure 4.11 with red diamonds. Both the DDL and dd samples had a measured macroscopic fracture of 37° - 39° for those samples that had an obvious shear localization that formed. The minimum values for each sample were plotted with blue squares in Figure 4.11.

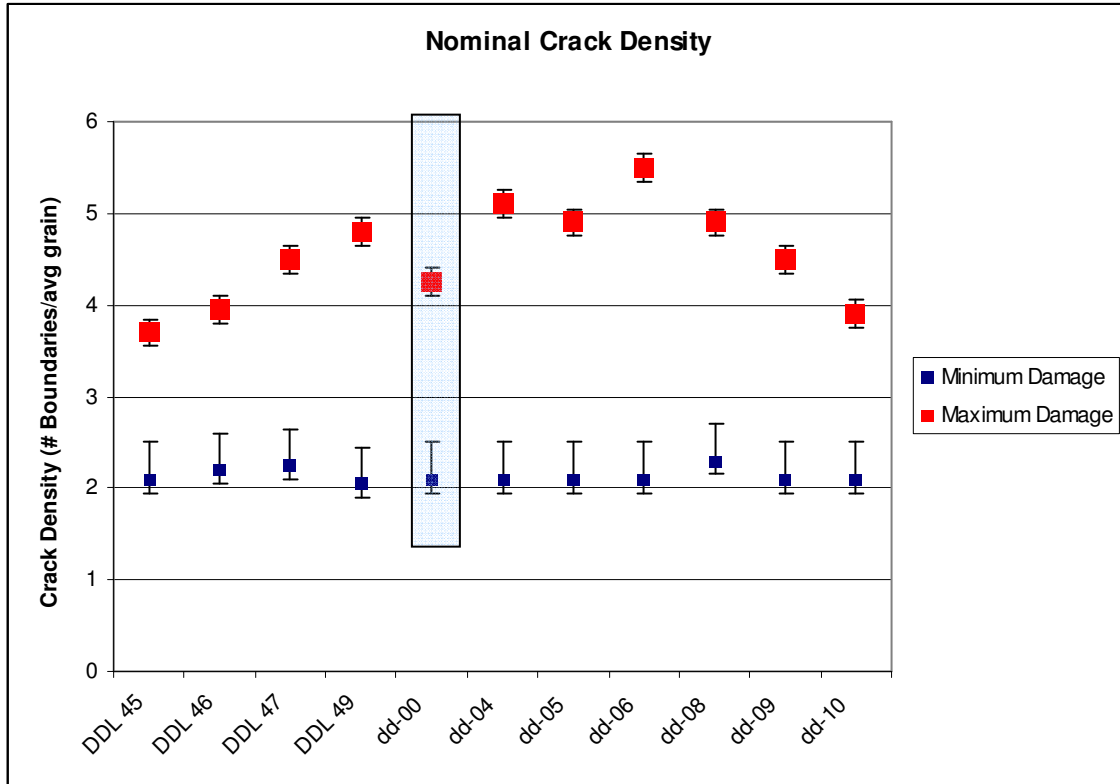


Figure 4.11: Nominal crack density of all samples. The areas of maximum damage were analyzed at all angles and the maximum crack density of all of these values was chosen to identify the maximum amount of damage in that portion of the thin section. In regards to the minimum values for each sample, a crack density of 2 indicates that there is no damage to the grain since this represents 2 edges per grain. The minimum damaged areas were averaged over all angles since there was no preferred damage orientation. The shaded area is the undeformed sample dd-00 (Tamarkin and Zhu, 2009).

A crack density of 2 indicates that there is no damage to the grain since this represents 2 edges per grain. It is also important to note that the minimum damage value have larger error bars than the maximum damaged areas. This is because the minimum damaged areas were averaged over all angles since there was no preferred damage orientation. While all of the samples have areas of damage, the maximum amount of damage within the DDL samples is associated with DDL49, deformed at 200 MPa. While DDL47 was also deformed at 200 MPa it was unloaded at a higher differential

stress and as a result it incurred less damage and has a lower maximum crack density. Within the dd samples, dd-04, dd-05, dd-06 and dd-08 had the maximum amount of damage and were all allowed to fail completely. Samples dd-04 (deformed at a strain rate of $1.8 \times 10^{-6} \text{ s}^{-1}$) and dd-06 ($2.5 \times 10^{-6} \text{ s}^{-1}$) show greater maximum damage density when compared to samples dd-05 and dd-08 which were strained at a rate of $5.5 \times 10^{-6} \text{ s}^{-1}$. This indicates that the slower the strain rates the greater the maximum amount of damage the sample experiences. As for samples dd-09 and dd-10, which were stopped at peak differential stress, their maximum damage was comparable with the control dd-00, but the damage index shows that although there was no coalescence of microscopic failures into a macroscopic failure, there is a much more widespread amount of microstructural damage.

The lack of macroscopic shear fracture in samples dd-09 and dd-10 (Figure 4.7) in conjunction with the low crack density observed in these 2 samples (Figure 4.11) implies that the macroscopic failure may be associated with a critical extent of microscopic damage. Damage parameters such as crack density obtained in this study provide useful constraints in modeling brittle faulting process (i.e., Hamiel et al. 2005), which may lead to new physical insights into the precursory phenomena associated with earthquakes.

Chapter 5: Conclusions

Dilatancy seems to be a key feature to better understand the point at which a rock will fail macroscopically. In granular materials, dilatancy can be attributed to the changes in packing of the grains during their relative movement and also the generation of microcracks within the grains. To investigate the brittle deformation of porous sandstones, a new lateral relaxation loading path was used and proven to be an effective tool to study the post-yielding behavior of rocks damaged by brittle failure. This loading path improves upon the conventional loading path by controlling the failure of the sample so that the post-yielding deformation process can be analyzed. The microstructures of a total of ten samples, deformed under the new loading path, were analyzed using a damage index and an automated crack density analysis which was developed specifically for this study. These analyses allowed successful mapping of the brittle failure envelope, and will allow further investigation of precursory phenomena in porous rocks. The experimental data implied that there was a critical dilatancy parameter that marks the onset of macroscopic failure. The results from these experiments indicate that the development of macroscopic fracture is associated with a damage threshold and could prove useful in advancing the understanding of the mechanics of brittle faulting of rock. The crack density parameter obtained in this study may assist other researchers and modelers by providing them with experimentally determined constraints on the damage parameters used in theoretical models.

This new loading path will be useful to represent some Earth processes where the effective pressure increases as a result of a decrease in confining pressure and an increase

in pore pressure such as rapid uplift or pore pressure increase in an accretionary wedge due to impermeability within the wedge.

It is known that pressure seals can form within a rock by the redistribution of fluids within the solution. If this were to occur at or near the boundary of a fault fluid within the fault cannot communicate with the pore space of the surrounding rock and result in an undrained condition. The over pressurized fluids within the fault would effectively reduce the amount of shear stress required for the rock to fail (Blanpied et al. 1992 and Rice 1992). A key geologic location to study this potentially undrained and high pore pressure environment is in subduction environments. During a great earthquake in a subduction environment, the outer wedge is pushed into a compressively critical state where there is a general increase in the basal and internal stresses as well as an increase in the pore fluid pressure (Wang and Hu, 2006). While the plate is subducting, the base of the overriding plate is eroded but the subduction of a seamount would entrain large quantities of fluid rich sediment. The damage caused by erosion may prevent the accumulation of elastic strain energy and elevated pore pressure may reduce the effective normal stress (Mochizuki et al. 2008 and Von Huene 2004) potentially forcing the rock to failure.

This mechanism is believed by some researchers to cause tremors and silent slip along subduction zones such as Cascadia and Japan. The undrained fluids contained within the sediment can cause an increase in the pore pressure (Rogers and Dragert 2003, and Dragert et al. 2001) as the loading conditions of the sediment within the wedge change, thus successfully decreasing the effective mean stress and slowly forcing the material into the failure criterion.

Considering the long duration and mobility of the tremor activity, the generation of tremors may also be related to the movement of fluid in the subduction zone. The fluids may be carried down with the slab in the aqueous state or the subducting slab may liberate aqueous fluid by dehydration. This may result in large amounts of fluid moving to the slab surface. Depending on the depth, the presence of fluid at the slab surface can change the fracture criterion of the rock by increasing the pore pressure and/or create new cracks through hydraulic fracturing. (Obara, 2002).

Continuous motion of the converging plates of the Cascadia margin produces tectonic loading of the locked sediment, eventually leading to earthquake rupture. But GPS data suggests that there is a seismic slip of large areas of deeper Cascadia subduction interface, below the seismogenic zone, between great earthquakes (Dragert et al. 2001). It is also important to note that there has been no obvious seismic trigger identified with these slow slip earthquakes. Some possible mechanisms relate to fluid movement within the subducting slab material. If the conditions of the tremor generation are unstable, the additional supply of fluid to an almost saturated system, or stimulation by nearby earthquake shaking, might trigger the observed tremor (Obara, 2002). Another possible tremor-generating mechanism is flow induced oscillation in channels transporting magmatic fluid (Obara, 2002). It is believed by Dragert et al. (2001) that these slow slip events may continue to propagate updip and evolve into a trigger mechanism for a great subduction earthquake.

The lateral relaxation loading path of this experimental study is intended to represent the geologic environments just described where an increase in pore pressure forces the material into the failure criterion by decreasing the effective mean stress.

Appendices

A.1 LVDT Calibration Plots

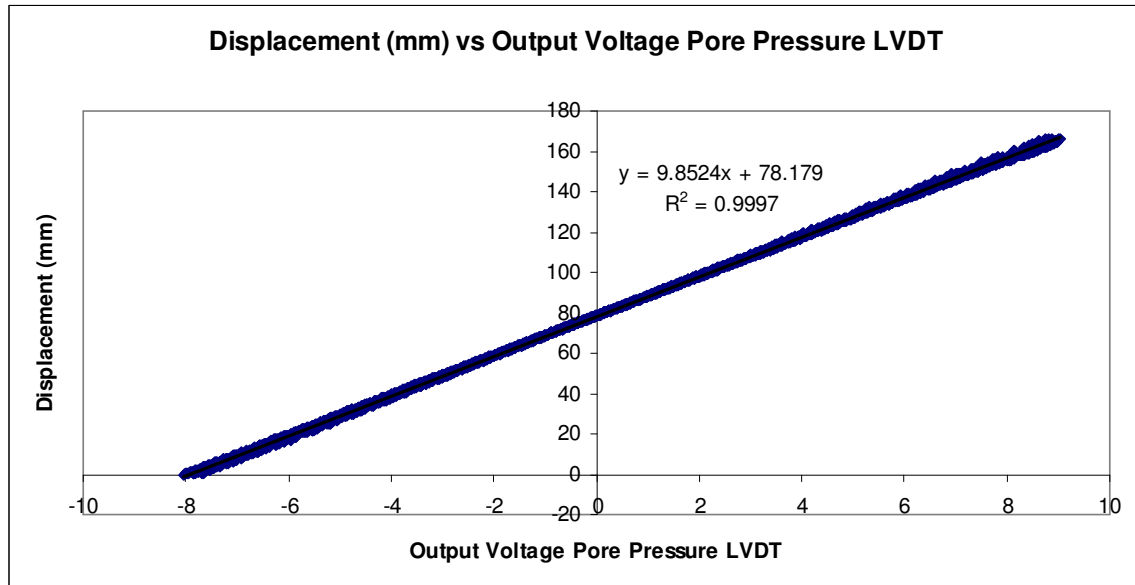
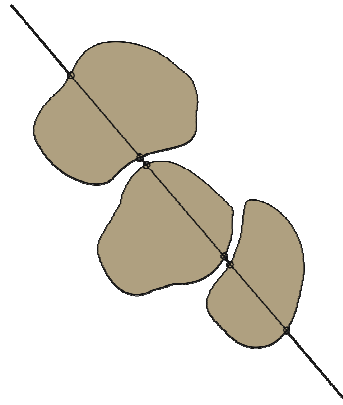


Figure A-1: Pore pressure intensifier LVDT calibration plot

A.2 Nominal Crack Density Calculation



$$NCD = \frac{\text{Feature Boundary Count}}{\text{Whole Grain Pixel Count}} \times \frac{\text{avg grain diameter}}{\text{grain}} \times \frac{1 \text{ pixel}}{\# \text{ micron}}$$

Figure A-2: Formula for calculation of nominal crack density

A.3 Standardization and Verification of Matlab technique

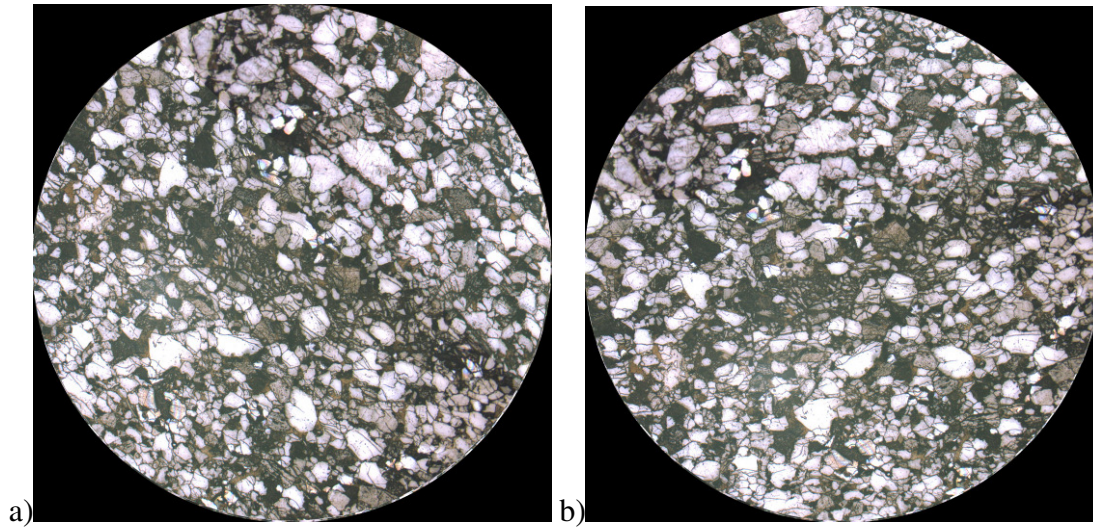


Figure A-3 a) and 3b: Random area selected for technique verification. b) Figure A-3a rotated 45° (Both on a black back ground).

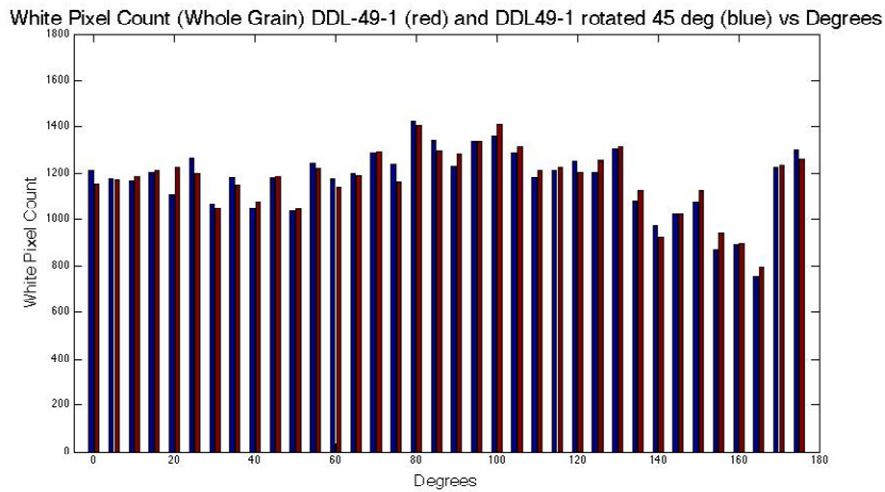


Figure A-3c: Comparison of image analysis from Figures A-3a and b Results are consistent indicating orientation of image does not affect crack counting software.

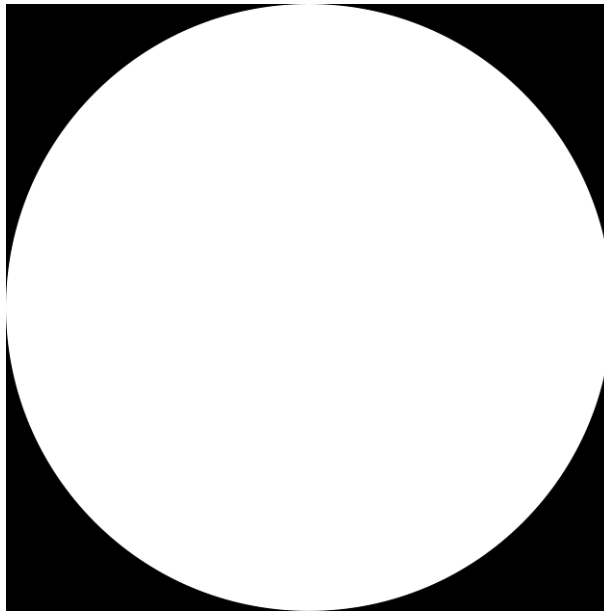


Figure A-4a: 2000 Pixel radius white circle.

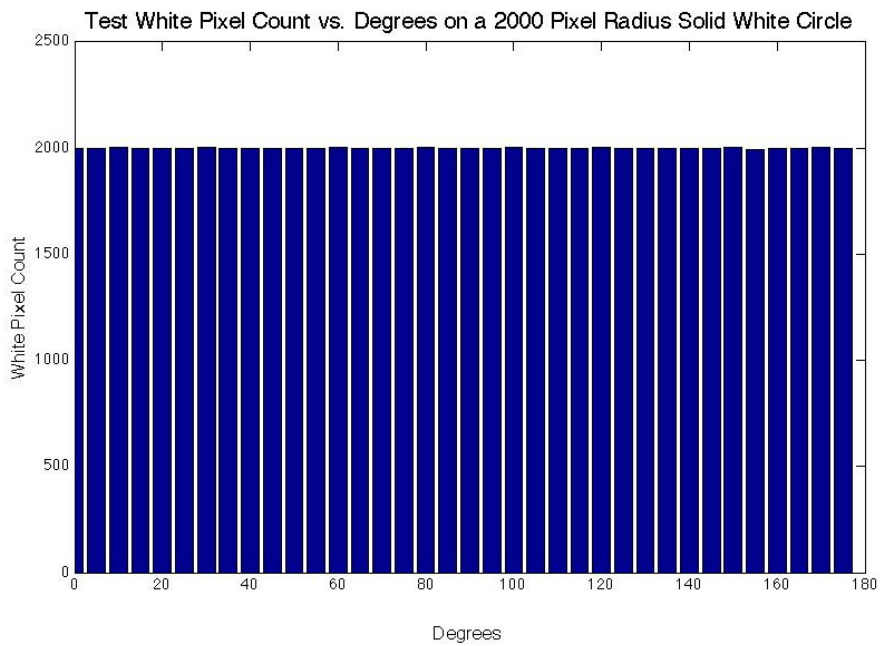


Figure A-4b: Matlab image analysis of 2000 Pixel radius white circle indicating 2000 pixels counted at all angles from 0-180°

A.4 Matlab code for image analysis: Grain Area

```
%Linehistogram creator
%Sums the number of times the line at a given angle crosses
white area
%in the image to be analyzed.

tic

%Request user input fir image to be analyzed
reply=input('Pick a file (reply must be in single quotes)')

Image=imread(reply); %Convert image into matrix
[x,map]=rgb2ind(Image,2); %Map image into two colors
binaryimage=logical(x); %Convert image to binary matrix
edgeimage=edge(binaryimage); %find the edges of the grains
in the matrix

%SAMPLE=edgeimage; %Pick between the edges or the
binary image (Wholegrains)
SAMPLE=binaryimage;

% 0=z
% 1=o
% 2=t
% 3=h
% 4=f
% 5=v
% 6=s
% 7=g
% 8=e
% 9=n

%test## is the array that contains the line at angle (XX)
%in degrees

M=SAMPLE+test0;
z=sum(M(:)==2);

M=SAMPLE+test5;
v=sum(M(:)==2);

M=SAMPLE+test10;
oz=sum(M(:)==2);

M=SAMPLE+test15;
ov=sum(M(:)==2);
```

```
M=SAMPLE+test20;
tz=sum(M(:)==2);

M=SAMPLE+test25;
tv=sum(M(:)==2);

M=SAMPLE+test30;
hz=sum(M(:)==2);

M=SAMPLE+test35;
hv=sum(M(:)==2);

M=SAMPLE+test40;
fz=sum(M(:)==2);

M=SAMPLE+test45;
fv=sum(M(:)==2);

M=SAMPLE+test50;
vz=sum(M(:)==2);

M=SAMPLE+test55;
vv=sum(M(:)==2);

M=SAMPLE+test60;
sz=sum(M(:)==2);

M=SAMPLE+test65;
sv=sum(M(:)==2);

M=SAMPLE+test70;
gz=sum(M(:)==2);

M=SAMPLE+test75;
gv=sum(M(:)==2);

M=SAMPLE+test80;
ez=sum(M(:)==2);

M=SAMPLE+test85;
ev=sum(M(:)==2);

M=SAMPLE+test90;
nz=sum(M(:)==2);

M=SAMPLE+test95;
nv=sum(M(:)==2);

M=SAMPLE+test100;
ozz=sum(M(:)==2);

M=SAMPLE+test105;
ozv=sum(M(:)==2);
```

```
M=SAMPLE+test110;  
ooz=sum(M(:)==2);
```

```
M=SAMPLE+test115;  
oov=sum(M(:)==2);
```

```
M=SAMPLE+test120;  
otz=sum(M(:)==2);
```

```
M=SAMPLE+test125;  
otv=sum(M(:)==2);
```

```
M=SAMPLE+test130;  
ohz=sum(M(:)==2);
```

```
M=SAMPLE+test135;  
ohv=sum(M(:)==2);
```

```
M=SAMPLE+test140;  
ofz=sum(M(:)==2);
```

```
M=SAMPLE+test145;  
ofv=sum(M(:)==2);
```

```
M=SAMPLE+test150;  
ovz=sum(M(:)==2);
```

```
M=SAMPLE+test155;  
ovv=sum(M(:)==2);
```

```
M=SAMPLE+test160;  
osz=sum(M(:)==2);
```

```
M=SAMPLE+test165;  
osv=sum(M(:)==2);
```

```
M=SAMPLE+test170;  
ogz=sum(M(:)==2);
```

```
M=SAMPLE+test175;  
ogv=sum(M(:)==2);
```

```
DST=[z/cosd(0) v/cosd(5) oz/cosd(10) ov/cosd(15) tz/cosd(20)  
tv/cosd(25) hz/cosd(30) hv/cosd(35) fz/cosd(40) fv/cosd(45)  
vz/sind(50) vv/sind(55) sz/sind(60) sv/sind(65) gz/sind(70)  
gv/sind(75) ez/sind(80) ev/sind(85) nz/sind(90) nv/cosd(5)  
ozz/cosd(10) ozv/cosd(15) ooz/cosd(20) oov/cosd(25)  
otz/cosd(30) otv/cosd(35) ohz/cosd(40) ohv/cosd(45)  
ofz/sind(50) ofv/sind(55) ovz/sind(60) ovv/sind(65)  
osz/sind(70) osv/sind(75) ogz/sind(80) ogv/sind(85)]
```

```
x=[0:5:175];
```

```

mean(DST)
std(DST)

bar(x,DST)
xlabel('Degrees','FontSize',16);
xlim([-5 180]);
ylabel('White Pixel Count','FontSize',16);
ylim([0 1800]);
title('White Pixel Count (Whole Grain) SAMPLE vs
Degrees','FontSize',20);
toc

```

A.5 Matlab code for image analysis: Feature Boundary

```

%Linehistogram creator
%Sums the number of times the line at a given angle crosses
white area
%in the image to be analyzed.

tic

%Request user input fir image to be analyzed
reply=input('Pick a file (reply must be in single quotes)')

Image=imread(reply); %Convert image into matrix
[x,map]=rgb2ind(Image,2); %Map image into two colors
binaryimage=logical(x); %Convert image to binary matrix
edgeimage=edge(binaryimage); %find the edges of the grains
in the matrix

SAMPLE=edgeimage; %Pick between the edges or the binary
image (Wholegrains)
%SAMPLE=binaryimage;

% 0=z
% 1=o
% 2=t
% 3=h
% 4=f
% 5=v
% 6=s
% 7=g
% 8=e
% 9=n

```

```
M=SAMPLE+test0;
z=sum(M(:)==2);

M=SAMPLE+test5;
v=sum(M(:)==2);

M=SAMPLE+test10;
oz=sum(M(:)==2);

M=SAMPLE+test15;
ov=sum(M(:)==2);

M=SAMPLE+test20;
tz=sum(M(:)==2);

M=SAMPLE+test25;
tv=sum(M(:)==2);

M=SAMPLE+test30;
hz=sum(M(:)==2);

M=SAMPLE+test35;
hv=sum(M(:)==2);

M=SAMPLE+test40;
fz=sum(M(:)==2);

M=SAMPLE+test45;
fv=sum(M(:)==2);

M=SAMPLE+test50;
vz=sum(M(:)==2);

M=SAMPLE+test55;
vv=sum(M(:)==2);

M=SAMPLE+test60;
sz=sum(M(:)==2);

M=SAMPLE+test65;
sv=sum(M(:)==2);

M=SAMPLE+test70;
gz=sum(M(:)==2);

M=SAMPLE+test75;
gv=sum(M(:)==2);

M=SAMPLE+test80;
ez=sum(M(:)==2);

M=SAMPLE+test85;
```

```
ev=sum(M(:)==2);

M=SAMPLE+test90;
nz=sum(M(:)==2);

M=SAMPLE+test95;
nv=sum(M(:)==2);

M=SAMPLE+test100;
ozz=sum(M(:)==2);

M=SAMPLE+test105;
ozv=sum(M(:)==2);

M=SAMPLE+test110;
ooz=sum(M(:)==2);

M=SAMPLE+test115;
oov=sum(M(:)==2);

M=SAMPLE+test120;
otz=sum(M(:)==2);

M=SAMPLE+test125;
otv=sum(M(:)==2);

M=SAMPLE+test130;
ohz=sum(M(:)==2);

M=SAMPLE+test135;
ohv=sum(M(:)==2);

M=SAMPLE+test140;
ofz=sum(M(:)==2);

M=SAMPLE+test145;
ofv=sum(M(:)==2);

M=SAMPLE+test150;
ovz=sum(M(:)==2);

M=SAMPLE+test155;
ovv=sum(M(:)==2);

M=SAMPLE+test160;
osz=sum(M(:)==2);

M=SAMPLE+test165;
osv=sum(M(:)==2);

M=SAMPLE+test170;
ogz=sum(M(:)==2);

M=SAMPLE+test175;
```

```
ogv=sum(M(:)==2);
```

```
DST=[z/cosd(0) v/cosd(5) oz/cosd(10) ov/cosd(15)  
tz/cosd(20) tv/cosd(25) hz/cosd(30) hv/cosd(35) fz/cosd(40)  
fv/cosd(45) vz/sind(50) vv/sind(55) sz/sind(60) sv/sind(65)  
gz/sind(70) gv/sind(75) ez/sind(80) ev/sind(85) nz/sind(90)  
nv/cosd(5) ozz/cosd(10) ozv/cosd(15) ooz/cosd(20)  
oov/cosd(25) otz/cosd(30) otv/cosd(35) ohz/cosd(40)  
ohv/cosd(45) ofz/sind(50) ofv/sind(55) ovz/sind(60)  
ovv/sind(65) osz/sind(70) osv/sind(75) ogz/sind(80)  
ogv/sind(85)]
```

```
x=[0:5:175];  
mean(DST)  
std(DST)  
bar(x,DST)  
xlabel('Degrees','FontSize',16);  
xlim([-5 180]);  
ylabel('White Pixel Count','FontSize',16);  
ylim([0 150]);  
title('White Pixel Count (Edge) SAMPLE vs  
Degrees','FontSize',20);  
toc
```

References

- Allegre, C.J., Le Mouel, J.L., and Provost A. (1982). Scaling rules in rock fracture and possible implications for earthquake prediction, *Nature*, v. 297, p. 47-49.
- Andrews, J. (1976). Rupture velocity of plane strain shear cracks, *Journal of Geophysical Research*, v. 81, p. 5679-5687.
- Bakun, W.H., and Lindh, A.G. (1985). The Parkfield, California, earthquake prediction experiment, *Science*, v. 229, p. 619-624.
- Bakun, W. H., and T. V. McEvilly (1984). Recurrence models and Parkfield, California, earthquakes, *J. Geophys. Res.*, v. 89, p. 3051– 3058.
- Baud, P., Zhu, W., Wong, T.-f. (2000). Fracture mode and weakening effect of water on sandstone, *Journal of Geophysical Research*, v. 105, p. 16,371-16,389.
- Blanpied M.L., Lockner D.A., and Byerlee J.D. (1992). An earthquake mechanism based on rapid sealing of faults, *Nature*, v. 358, p. 574-576.
- Brace, W.F. (1964). Brittle fracture of rocks. In *State of Stress in the Earth's Crust* (ed Judd). New York. American Elsevier Publishing Co., p111-180.
- Brace W.F., Paulding B.W. Jr, Scholz C. (1966). Dilatancy in the fracture of crystalline rocks, *Journal of Geophysical Research*, v. 71, p. 3939-3953
- Brace W.F. (1978). Volume changes during fracture and frictional sliding: a review, *Pure and Applied Geophysics*, v. 116, p. 603-614.
- Brace, W.F. and Orange, A.S. (1968). Electrical resistivity changes in saturated rock during fracture and frictional sliding, *Journal of Geophysical Research*, v. 73, p. 1433-1445.
- Brace, W.F. and Jones, A.H. (1971). Comparison of uniaxial deformation in shock and static loading of three rocks, *Journal of Geophysical Research*, v. 76, p. 4913-4921.
- Bridgeman P.W. (1949). Volume changes in the plastic stages of simple compression, *Journal of Applied Physics*, v. 20, p. 1241-1251.
- Bridgman P.W. (1958). *The physics of high pressure*, Bell and Sons ltd, London, p. 1-432.
- Brodsky, E.E., and Kanamori, H. (2001). Elastohydrodynamic lubrication of faults, *Journal of Geophysical Research*, v. 106, p 16357-16374.

- Cook, N.G.W. (1970). An experiment proving that dilatancy is a pervasive volumetric property of brittle rock loaded to failure, *Rock Mechanics* 2.
- Das, S. (1981). Three-dimensional spontaneous rupture propagation and implications for the earthquake source mechanism. *Geophysical Journal of the Royal Astronomical Society*, v. 67: p. 375–393.
- Davis J.R. and Allen P. (1990). *ASM Metals Handbook* 10th ed., v. 2, ASM International, USA, p. 70-71.
- Dobie, and Isaac. (1950). *Electric Resistance Strain Gauges*. English Universities Press Limited, London, 1950, p. 83.
- Dragert H., Wang K., and James T. (2001). A silent slip event on the deeper Cascadia subduction interface, *Science*, v. 292, p. 1525-1528.
- Duff, P.McL.D. and Smith, A.J. (1992). *Geology of England and Wales*, Geological Society of London, p. 78.
- Fenoglio, M.A., Johnston, M.J.S., and Byerlee, J. (1995). Magnetic and electric fields associated with changes in high pore pressure in fault zones – Application to the Loma Prieta ULF emissions, *Journal of Geophysical Research*, v. 100, p. 12951–12958.
- Frank F.C. (1965). On dilatancy in relation to seismic sources. *Review of Geophysics*, v. 3, p. 485-503.
- Geller, R.J. (1997). Earthquake prediction: A critical review, *Geophys. J. Int.*, v. 131, p. 425-450.
- Gilbert, G.K. (1909). Earthquake forecasts, *Science*, v. 29, p121-138.
- Hamiel, Y., Lyakhovsky, V., Agnon, A. (2005). Poroelastic damage rheology: Dilation, compaction, and failure of rocks, *Geochemistry Geophysics Geosystems*, v. 6, p. 1-9.
- Haskell, N.A. (1966). Total energy and energy spectral density of elastic wave radiation from propagating faults. Part II. A statistical source model, *Bulletin of the Seismological Society of America*, v. 56, p. 125-140.
- Hays and Horowitz. (1989). *The Student Manual for The Art of Electronics*. Cambridge University Press, New York, p. 175-232.
- Horowitz and Hill. (1989). *The Art of Electronics*: Cambridge University Press, New York, p. 1-251.

- Ismail I.A.H. and Murrell S.A.F. (1976). Dilatancy and the strength of rocks containing pore water under undrained conditions, *Geophysical Journal Royal Astronomical Society*, v. 44, p 107-134.
- Johnston, M.J.S. (1997). Review of electric and magnetic fields accompanying seismic and volcanic activity, *Surveys in Geophysics*, v. 18, p. 441-475.
- Kagan, Y.Y., and Jackson, D.D. (2000). Probabilistic forecasting of earthquakes, *Geophys. J. Int.*, v. 143, p. 438-453.
- Kagan, Y.Y. and Knopoff, L. (1987). Statistical short-term earthquake prediction. *Science*, v. 236, p. 1563-1567.
- King, C.Y. (1986). Gas geochemistry applied to earthquake prediction: An overview. *Journal of Geophysical Research*, v. 91, p. 12269-12281.
- Klein, E., Baud P., Reuschle T., and Wong T.F. (2001). Mechanical behavior and failure mode of bentheim sandstone under triaxial compression, *Phys. Chem. Earth (A)*, v. 26, p. 21-25.
- Lachenbruch, A. H. (1980). Frictional heating, fluid pressure and the resistance to fault motion, *Journal of Geophysical. Research*, v. 85, p. 6097-6112.
- Lockner, D., Byerlee, J.D., Kuksenko, V., Ponomarev, A., Sidorin, A. (1992). Observations of quasistatic fault growth from acoustic emission, *Fault Mechanics and Transport Properties of Rocks*, edited by Evans, B., and Wong, T.-f., Academic Press , San Diego, California, p. 3-32.
- Main, I. (1996). Statistical physics, seismogenesis, and seismic hazard, *Reviews of Geophysics*, v. 34, p. 433-462.
- Measurement Group Inc. (1992). *Instruction Manual: Model 2100 Strain gage conditioner and amplifier system*, TD publishing, USA, p. 1-22.
- Menéndez, B., Zhu, W., Wong, T.-f. (1996). Micromechanics of brittle faulting and cataclastic flow in Berea sandstone, *Journal of Structural Geology*, v. 18, p. 1-16.
- Mochizuki K. Yamada T. Shinohara M. et al. (2008). Weak interplate coupling by seamounts and repeating M~7 Earthquakes, *Science*, v. 321, p. 1194-1197.
- Mohr, O. (1882). Ueber die Darstellung des Spannungszustandes und des Deformationszustandes eines Korperelementes und uber die Anwendung derselben in der Festigkeitslehre, *Civil Engenieur*, v. 28, p. 113-156.
- Muir-Wood, R. and King, G.P.K. (1993). Hydrological signatures of earthquake strain, *Journal of Geophysical Research*, v. 98, p. 22,035-22068.

- Murray and Miller. (1992). *The Bonded Electrical Resistance Strain Gage*, Oxford University Press, New York, p. 1-118.
- Nasuno, S., Kudrolli, A., and Gollub, J.P. (1997). Friction in granular layers: Hysteresis and precursors, *The American Physical Society: Physical Review Letters*, v. 79, p. 949-952.
- Obara K. (2002). Nonvolcanic deep tremor associated with subduction in southwest Japan, *Science*, v. 296, p.1679-1680.
- Park, S.K. (1991). Monitoring changes of resistivity prior to earthquakes in Parkfield, California, with telluric arrays, *Journal of Geophysical research*, v. 96, p. 14,211–14,237.
- Parry, R.H.G. (1995). *Mohr Circles, Stress Paths and Geotechnics*, E&FN Spon publishing, United Kingdom, p. 1-217.
- Patterson M.S. and Wong T-f. (2005). *Experimental Rock Deformation-The Brittle Field* 2nd edition, Springer-Verlag Berlin Heidelberg, p. 1-265.
- Reid, H. F. (1910). *The Mechanics of the Earthquake*, Vol. II of *The California Earthquake of April 18, 1906*, Report of the State Earthquake Investigation Commission, A.C. Lawson, Chairman, Carnegie Institution of Washington Publication 87, p. 192.
- Roeloffs, E. A. (1998). Persistent water level changes in a well near Parkfield, California, due to local and distant earthquakes, *Journal of Geophysical Research*, v. 103, p. 869-889.
- Schock, R.N. and Heard, H.C. (1974). Static mechanical properties and shock loading response of granite, *Journal of Geophysical Research*, v. 79, p. 1662-1666.
- Scholz, C.H. (2002). *The Mechanics of Earthquakes and Faulting*, 2nd edition, Cambridge university press, United Kingdom, p. 1-414.
- Scholz C.H. and Koczyński T.A. (1979). Dilatancy anisotropy and the response of rock to large cyclic loads, *Journal of Geophysical Research*, v. 84, p. 5525- 5534.
- Scholz, C. H., L. R. Sykes, and Y. P. Aggarwal. (1973). Earthquake prediction: A physical basis, *Science*, v. 181, p. 803-810.
- Shimazaki K. and Nakata T. (1980). Time-predictable recurrence model for large earthquakes, *Geophysical Research Letters*, v. 7, p 279-282.
- Tamarkin, T. and Zhu, W. (2009). Progressive microscopic damage and the development

- of macroscopic fractures in porous sandstones, *Eos Trans. AGU*, 90(52), Fall Meet. Suppl., Abstract T54A-04.
- Turcotte, D. L. (1991). Earthquake prediction, *Annual Review Earth Planetary Science*, v. 19, p. 263-281.
- Vishay Micro-Measurements. (2003). Strain Gage Dimensions, Vishay, Document number 11505.
- Wakita, H. (1975). Water wells as possible indicators of tectonic strain, *Science*, v. 189, p. 553-555.
- Waller, R.M., Thomas, H.E., and Vorhis, R.C. (1965). Effects of the Good Friday earthquake on water supplies, *Journal of American Water Works Association*, v. 57, p 123-131.
- Walsh, J. (1965). The effect of cracks on the compressibility of rock, *Journal of Geophysical Research*, v. 70, p. 381-389.
- Wawersik, W., and Brace, W.F. (1971). Post-failure behavior of a granite and a diabase. *Rock Mech.* v.3, p. 61-85.
- Whitehead, R.L., Harper R.W., and Sisco, H.G. (1984). Hydrologic changes associated with the October 28, 1983, Idaho earthquake, *Pure and Applied Geophysics*, v. 122, p. 280-293.
- Wilson and Kester. (2009). Test and Measurement. Newnes Elsevier, Burlington MA, p. 414.
- Wong, T.-f., David, C. and Zhu, W. (1997). The transition from brittle faulting to cataclastic flow in porous sandstones: mechanical deformation, *Journal of Geophysical Research*, v.102, p. 3009-3025.
- Wu, X.Y., Baud, P., Wong, T.-f. (2000). Micromechanics of compressive failure and spatial evolution of anisotropic damage in Darley Dale sandstone. *Int. J. Rock Mech. Min. Sci.* v.37, p. 143–160.
- Wood, H. O., and Gutenberg, B. (1935). Earthquake prediction, *Science*, v.82, p. 219-220.
- Zhu, W., P. Baud and T.-f. Wong. (2003). Dilatancy and post-yielding behavior in porous sandstones: A new loading path, *Proceedings of the 39th U.S. Rock Mechanics Symposium*, P.J. Culligan, H.H. Einstein and A.J. Whittle (editors), Soil and Rock America, p. 437-444.